

**ENHANCED 3D STRUCTURAL INTERPRETATION
OF THE EASTERN ARKOMA FOREDEEP**

A Thesis

Presented to

the Faculty of the Department
of Earth and Atmospheric Sciences

University of Houston

In Partial Fulfillment

of the Requirements for the Degree of
Master of Science in Geophysics

By

Ryan B. Rogers

December, 2012

**ENHANCED 3D STRUCTURAL INTERPRETATION
OF THE EASTERN ARKOMA FOREDEEP**

Ryan B. Rogers

APPROVED:

Dr. Michael Murphy, Chairman

Dr. Jolante Van Wijk

Dr. Chris Liner

University of Arkansas 72701

James Lemaux

Southwestern Energy 77032

**Dr. Mark A. Smith, Dean, College of Natural
Sciences and Mathematics**

Acknowledgements

Foremost, I would like to express my sincere gratitude to all the individuals whose encouragement and assistance deserve special recognition, without whom I would never have been able to complete this thesis or degree. While this has been a long endeavor in which I called upon the assistance of countless individuals and groups, to these individuals and groups I would like to dedicate this thesis.

It would not have been possible to finish without the love and support of my wonderful wife Jennifer, whom has supported me from the beginning and reminds me daily that I am capable of doing anything. To Mom, Dad, BJ, and Robert, I am extremely grateful for all the love, encouragement, and prayer that you have given me over the past several years.

I would like to thank my advisor Dr. Michael Murphy for taking me on as a student late in my graduate studies and helping me finish strong. I would like to thank Dr. Chris Liner for starting me off on the right foot towards accomplishing my goals. I would also like to thank Dr. Jolante Van Wijk for her encouragement throughout the writing process.

This study would not have been possible without funding from Southwestern Energy as well as the guidance from the individuals that make the company what it is. First and foremost, I would like to thank my mentor Jim Lemaux, whose technical expertise and cheerful attitude have made this study meaningful and enjoyable. Also to my managers, Randy Wells, Gary Bajgier, Kristin Zembeck-England, John Jeffers, Joel Greer, and Damian Friend, who have always supported me and helped me understand that finishing my degree was my first priority towards becoming a successful geoscientist. To all the geoscientists in the Fayetteville Shale Division that discussed theories and workflows with me during this study, for your technical expertise and

patience I am grateful. Finally, to SWN Fellowship, thank you for all the prayer and support over the last two years; I could not have done it without you.

**ENHANCED 3D STRUCTURAL INTERPRETATION
OF THE EASTERN ARKOMA FOREDEEP**

An Abstract of a Thesis

Presented to

the Faculty of the Department
of Earth and Atmospheric Sciences

University of Houston

In Partial Fulfillment

of the Requirements for the Degree of
Master of Science in Geophysics

By

Ryan B. Rogers

December, 2012

Abstract

The Arkoma Basin is a foreland basin located in the southern midcontinent of the United States along the Ouachita Fold and Thrust Belt. This study focuses on a portion of the foredeep depozone in the eastern portion of the basin. Three-dimensional seismic data provided by Southwestern Energy (SWN) were used to develop a high resolution picture of the subsurface that was incorporated into the regional tectonic framework of the southeastern portion of North America. My interpretation shows that there are two separate structural systems present in the eastern Arkoma Basin indicated by two sets of faults. The two fault sets are distinguished by a deep set of high-angle normal faults and a shallow set of lower-angle normal faults. The deep set of faults predominantly trend NE/SW in the eastern portion of the study area and NW/SE in the western portion of the study area. The NW/SE faults are interpreted to have experienced a large amount of strike-slip. Shallow faults uniquely trend in an E/W direction. The orientation of faults suggests that dip-slip along the deep set of faults did not directly drive the formation of the shallow faults. Rather, I interpret that reactivation of the deep faults in an oblique-slip motion is responsible for generating the en echelon array of faults structurally above the reactivated deep faults.

Relative timing of faulting for the study area began with deep, down-to-the-southeast normal terrace faults. Continued deformation progressed with dextral-slip along the central NW/SE-trending deep fault. Reactivation of NE/SW-trending deep faults in a dextral-slip motion generated the en echelon array of faults in the shallow section. Regional extension is interpreted to generate the final amount of slip observed along all deep faults and the shallow faults structurally above. Two structural models were developed using the relative timing

mentioned to illustrate deformation in the study area. The first structural model considers post-Ouachita deformation and includes effects from Mesozoic rifting. The second structural model attempts to follow past literature and consider deformation only up to Late Pennsylvanian time.

Contents

1 Introduction	1
2 Geologic History	
2.1 Proterozoic Tectonic Evolution of Southeastern North America	4
2.2 Tectonic Evolution and Depositional Environment of the Ouachita Orogeny and Arkoma Basin.....	6
2.3 Arkoma Surface Expression	9
3 Methods	
3.1 General.....	11
3.2 Horizons	11
3.3 Synthetic Ties and Manual Horizon Interpretation	16
3.4 Fault Interpretation.....	28
3.5 Gridding and Depth Modeling.....	32
3.6 Isochores	34
4 Interpretation and Results	
4.1 Structural Geology	34
4.1.1 Deep Structure	35
4.1.2 Shallow Structure	46
4.1.3 Fault Length and Displacement Implications.....	53
4.2 Linking the Deep and Shallow Structure	56
4.3 Relative Timing.....	60
4.4 Structural Model	64
5 Discussion	
5.1 Implications for the Tectonic Evolution of the Arkoma basin	68
5.2 Reactivation, Crustal Loading, and Crustal Flexure	72
6 Conclusion.....	76
7 References	78

1 Introduction

The Arkoma Basin is a foreland basin located in the southern midcontinent of the United States situated along the Oklahoma-Arkansas border. Bounded by the Ozark Dome to the north, the Cherokee Platform to the west, the Ouachita Mountains to the south, and the Reelfoot Rift to the east, the Arkoma Basin is one in a series of foreland basins associated with crustal thickening within the Ouachita fold-thrust belt (figure 1.1). The 3D Seismic interpretation and structural analysis presented in this thesis both confirms and better constrains the current understanding of the structural evolution of the basin.

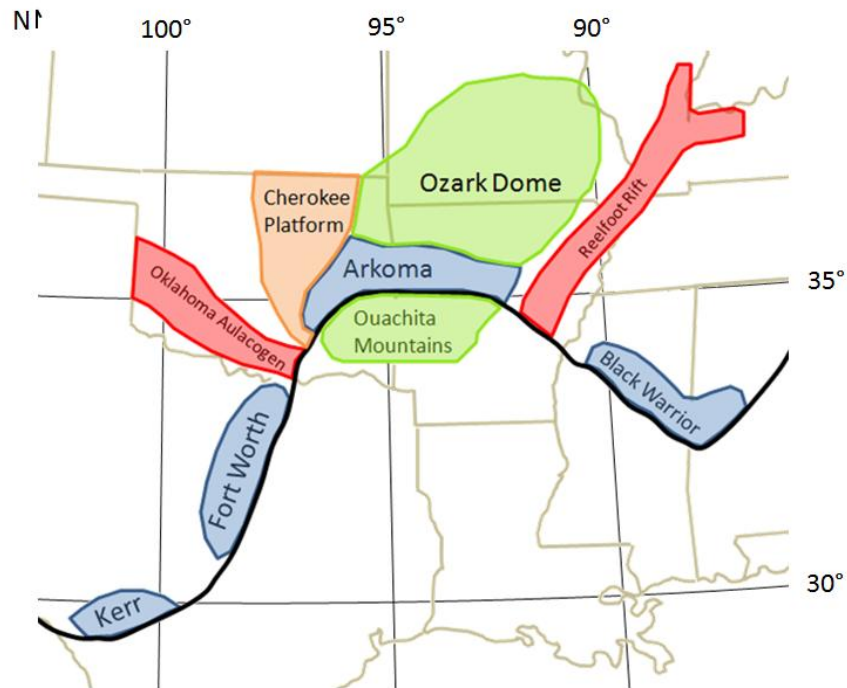


Figure 1.1: Delineation of the northern extent of the Ouachita Fold and Thrust Belt along with associated basins and bounding structural features of the Arkoma Basin (latitude and longitude lines included). Black – northern extent of Ouachita Fold and Thrust Belt, blue – associated foreland basins, red – tectonic features indicating rifting, green – structural highs indicating orogenic features and cratonic uplift, orange - Cherokee Platform.

Previous work on the tectonic evolution of the southern midcontinent is consistent with observations made during structural interpretation. Past studies propose a structural history characterized by Late Proterozoic to Early Cambrian rifting of the southeastern margin of North America (Houseknecht, 1986; Thomas, 1989; Van Arsdale and Schweig, 1990) followed by Late Mississippian to Early Pennsylvanian convergence of an island arc or continental plate (Houseknecht, 1986). The previously formed passive margin is interpreted to have controlled the location and geometry of thrusting during the obduction of the Ouachita Fold Belt (Thomas, 1977). Crustal loading and flexural bending during obduction generated large down-to-the-south normal faults that cut the passive margin structure (Houseknecht, 1986) producing accommodation space for Arkoma basin fill. Synorogenic deposition marks timing of the Ouachita Orogeny in the western portion of the basin (Houseknecht, 1986). Orogenesis continued throughout the Atokan and into the Desmoinesian (Houseknecht, 1986). However, by looking at the geological map of Arkansas (Haley et al., 1976), strata that were deposited within the eastern portion of the basin during this orogenic event have either been eroded or were never deposited. Therefore, any kinematic history archived in stratigraphic units younger than the Middle Atoka in the eastern Arkoma region has not been preserved. This thesis provides a 3D structural interpretation for the eastern portion of the Arkoma Basin that suggests a different kinematic history and timing than previously proposed. Seismic data indicates that the large normal faults have a differing orientation than the typical regional E/W-trending fault system. Also, seismic data suggests strike-slip displacement along NW-trending faults and subsequent normal faults with cross-cutting relationships.

The study area is located in north-central Arkansas just north of the Ouachita frontal thrusts (figure 1.2). Seismic data within the study area were acquired to help assist exploitation

of the Fayetteville Shale. Large data sets composed of surface seismic and well penetrations are becoming increasingly common for unconventional shale plays because of their large aerial extents. The study area consists of 800 square miles (2072 km²) of 3D surface seismic data that were acquired by Southwestern Energy (SWN) and multiple third-parties from 2006 to 2009. The 3D data consists of more than 20 individual surveys acquired with different acquisition parameters including differing acquisition geometries and orientations. The data were reprocessed to a north-south orientation with 110 ft (33.5 m) bin spacing in 2010 to enhance continuity. The merged data set was utilized for interpreting. The data set is a Pre-Stack Time Migrated (PSTM) volume. An interpretation of the 800 square miles (2072 km²) of 3D seismic was completed where data quality permitted.

Besides the Ouachita Mountains, Arkansas is often accused of having simple “pancake” geology. The subsurface, however, tells a different story. This research will attempt to take past interpretations using global scale tectonics and shallow crustal deformation to better understand the structural geology of the foredeep portion of the eastern Arkoma Basin. The scope of this thesis is to evaluate the current understanding of the tectonic evolution of the Arkoma Basin, add a more detailed subsurface interpretation of the eastern portion of the basin using 3D seismic, and consider potential post-Ouachita deformation in the development of the Arkoma foreland.

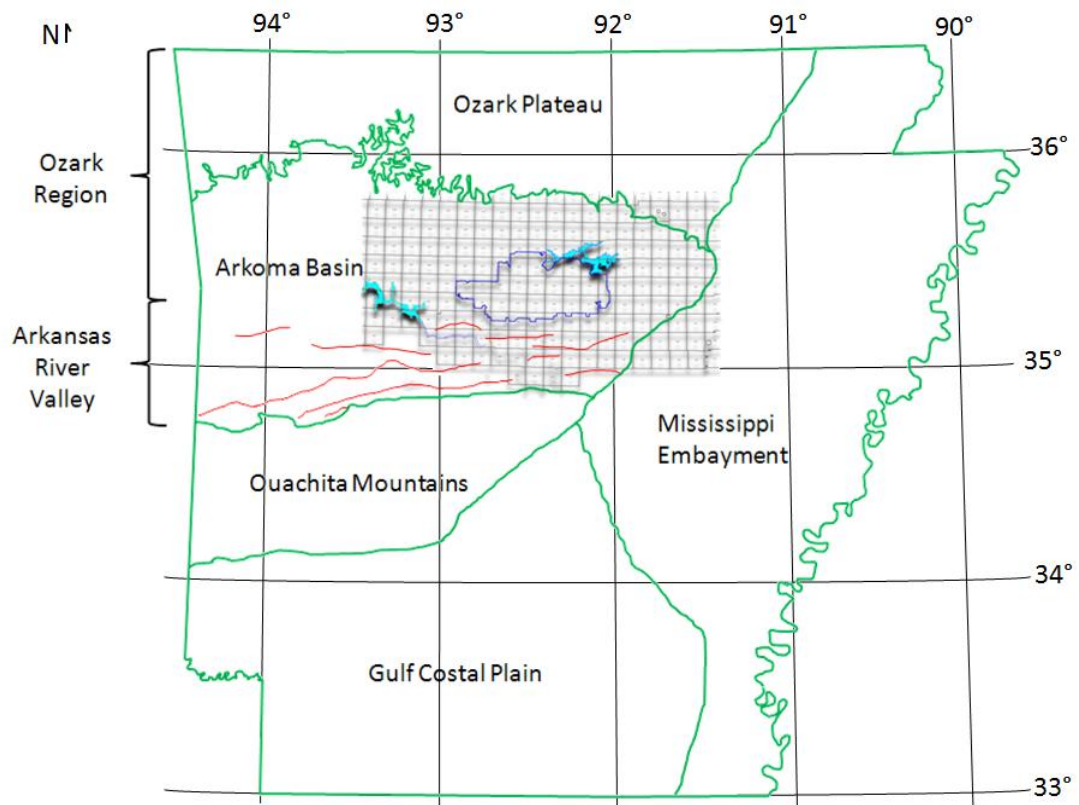


Figure 1.2: Study area with surrounding major geographic regions. Blue outline – study area, light blue – nearby major hydrological features, red – Ouachita frontal thrusts, black lines – latitude and longitude.

2 Geologic History

2.1 Proterozoic Tectonic Evolution of Southeastern North America

The southeastern continental margin of North America has experienced two major extensional events and a compressional event since the Proterozoic. The first extensional event is referenced in Whitmeyer and Karlstrom (2007). Whitmeyer and Karlstrom compiled extensive literature based on outcrop, borehole, and aeromagnetic data to characterize Proterozoic evolution in the southeastern continental margin of North America. The southeastern continental margin is characterized as a series of accreting juvenile volcanic arcs and oceanic

terrains followed by continental rifting (figure 2.1). The study area for this thesis is situated within the Granite-Rhyolite Province, which is interpreted to be 1.55-1.35 Ga juvenile crust and granitoids. Rifting associated with the breakup of Rodinia is hypothesized to have occurred around 0.535 Ga detaching the Argentine Precordillera and developing the Oklahoma Aulacogen and Reelfoot Rift.

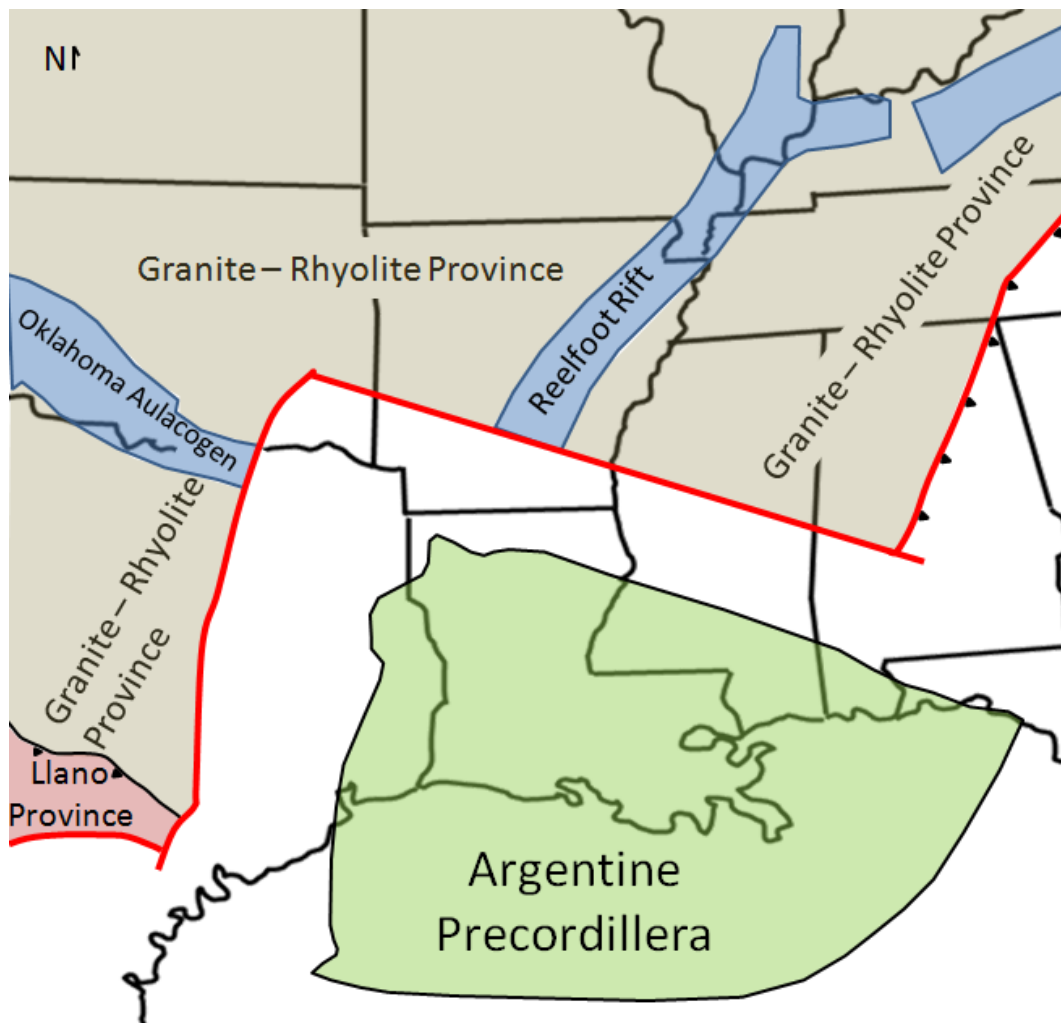


Figure 2.1: Simplified model showing the Proterozoic geology of the southern midcontinent of the United States; red line – continental rift boundary. (Figure modified from Whitmeyer and Karlstrom, 2007).

2.2 Tectonic Evolution and Depositional Environment of the Ouachita Orogeny and Arkoma Basin

The overall shape and position of the Ouachita Fold Belt and Arkoma Basin were hypothesized to have been controlled by the preexisting zigzag shape of the continental margin, generated from the initial rifting of the southeastern margin of North America (Thomas, 1977). The Arkoma Basin is an arcuate tectonic feature and was produced by an extensional structural regime north of the Ouachita Fold Belt. The transition from passive margin to foreland basin has been interpreted to have progressed through five distinct stages (figure 2.2). The transition is also represented by distinct changes in lithology from the Late-Mississippian to Early-Pennsylvanian section. A simplified stratigraphic column of the study area, based on interpreted horizons, is shown in figure 2.3. Late Precambrian to Early Paleozoic rifting was followed by alternating cycles of transgressive and regressive sequences and periodic uplifting of the Ozark dome, which generated the gentle, south sloping passive margin shelf that set the stage for depositing sequences of shallow-water carbonates and clastics up to the Atokan (Frezon and Glick, 1959). Near the Devonian or Early Mississippian, the Iapetus Ocean basin south of the North American continent began to close with the subduction of the North American plate under the continental margin Llanoria (Houseknecht, 1986). During the Late Mississippian, carbonates dominate the depositional environment with some intermittent influx of terrigenous clastics (Sutherland & Manger, 1979; Sutherland, 1988). Transition from predominantly carbonate to an increasing terrigenous clastic depositional environment progresses into the Early Pennsylvanian (Sutherland & Manger, 1979). By the Early Atokan, the ocean basin created by Precambrian-Cambrian rifting was consumed by the advancing accretionary prism to the South (Houseknecht, 1986). Beginning in the Middle Atokan, further subduction and flexural downwarping of the southern margin of the North American plate provided the tensional stress

needed to generate large down-to-the-south normal faults, increasing the accommodation space within the Arkoma basin (Sutherland, 1988). The rapid sedimentation rates associated with the increased accommodation space continued throughout the Middle Atokan (Sutherland 1988). Basin fill was derived from multiple sources including tectonic provinces southeast of the Ouachita trough, uplifted Ouachitas to the south, deltaic deposits from the Ozark dome to the north and continental interior to the west (Sutherland, 1988). Some of the faulting within the Arkoma basin potentially exhibited reactivation of the Early Precambrian to Early Paleozoic rifting (Houseknecht, 1986). Deformation from Late Atokan to Desmoinesian was characterized by foreland-style thrusting. The cessation of deformation occurred somewhere near or after the Desmoinesian (Houseknecht, 1986).

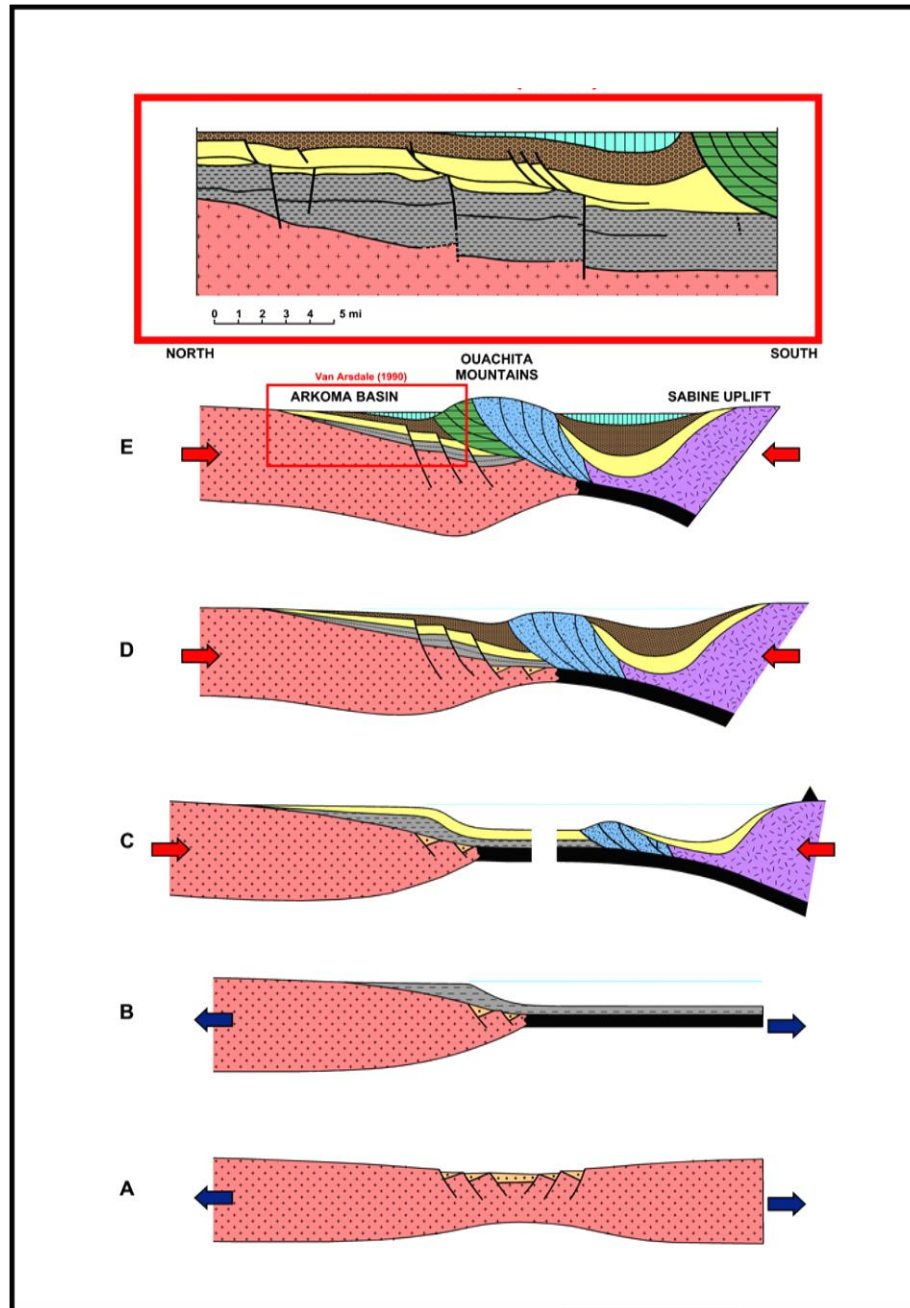


Figure 2.2: Cross-sections showing transition from passive margin to foreland basin of the southern margin of North America (Houseknecht, 1986) and zoom in of the foredeep and the northern portion of the wedge top depozones interpreted from regional 2D seismic lines (Van Arsdale and Schweig, 1990). (A) Late Precambrian-Early Paleozoic, (B) Late Cambrian-Early Mississippian, (C) Early Mississippian-Early Atokan, (D) Early-Middle Atokan, and (E) Late Atokan-Desmoinesian. The top box indicates the portion of the basin that was interpreted by Van Arsdale and Schweig and the focus area for this thesis. Key to colors: red = continental crust; orange = Basal Paleozoic strata; black = oceanic crust; gray = Upper Cambrian-Basal Mississippian strata; purple = Llanorian crust; blue = Ouachita subduction complex; yellow = Mississippian-Basal Atoka strata; black triangle = magmatic arc volcanoes; brown = Lower-Middle Atoka strata; green = Ouachita foreland thrust belt; teal = Upper Atokan-Desmoinesian strata. Figure modified from Houseknecht (1986) and Van Arsdale and Schweig (1990).

Age			Arkoma Foreland (Study Area)	Lithology
Paleozoic	Carboniferous	Lower Atokan	Sells	
			Orr	Upper
				Middle
				Lower
		Morrowan		
			Hale	Upper
				Middle
				Lower
				Basal
			Morrow	
	Mississippian	Chesterian	Fayetteville	
			Hindsville	
		Meramecian		
		Osagean		
	Cambrian - Devonian	Kinderhookian		
		Hunton		
		Simpson	St. Peter	
		Arbuckle		
	Precambrian			

Figure 2.3: Simplified stratigraphic column for study area; Arkoma foreland units based on horizons interpreted and units of interest from 3D seismic volume. Precambrian includes all four basement reflectors.

2.3 Arkoma Surface Expression

On the Arkansas side of the basin, the surface expression generated by the formation of the Arkoma basin is seen in the frontal Ouachitas, Arkansas River Valley, and the southern portion of the Ozarks (Haley et al. 1976). Moving from south to north, the basin's surface extent

is bounded on the south near the exposed Stanley Shale, Jackfork Sandstone, and Johns Valley Shale. The Stanley Shale is of Mississippian age; the Jackfork Sandstone and Johns Valley formations are of Pennsylvanian age and of the Morrowan series. All three formations have south-dipping thrust faults present, and contact the Early Atoka. The surface structure just north of the frontal Ouachitas exposes the Atokan formation and is characterized by broad, east-west trending synclines and narrow anticlines. Some thrusting is still present north of the frontal Ouachitas, striking generally east-west; however, no thrust faulting is present north of the Arkansas River where the surface formation is listed as Undifferentiated Atoka. Further north into the southern extent of the Ozark Plateau, the surface geology is littered with normal down-to-the-south faults generated from the extensional structural regime that formed the deep basin. These normal faults develop ridges of high relief and slopes that control the drainage of the Boston Mountains. Orientation of these normal faults generally strike east-west near the Arkansas-Oklahoma state line, northwest as they move further to the east, and northeast near the Mississippi Embayment. The surface expression is bounded on the north by the Mississippian Chesterian group that is also the vertical extent of the basin. The exposed Mississippian strata represent the relatively flat, stable shelf present before the formation of the basin. The erosion of the Mississippian carbonates and shales to the north has generated deep valleys which function as the watersheds for lakes and rivers within the southern Ozarks.

3 Methods

3.1 General

The data used to interpret the study area is a Pre-Stack Time Migrated (PSTM) seismic reflection volume. The processed data set was interpreted using a number of modules within the IHS Kingdom Suite software package. SynPAK was utilized to generate synthetic seismograms. Interpretation of time horizons between synthetics was carried out using 2d/3dPAK. Once a coarse interpretation for each time horizon was completed, a gridding function was used to interpolate and extrapolate to areas that were not manually interpreted. Fault interpretation was completed through two methods: manually interpreting fault intersections from cross-sectional inlines and crosslines as well as incorporating associated extractions from post-stack seismic attribute volumes. Depth conversion modeling was completed primarily using average velocities (in addition to one interval velocity). All depth and isochore maps on which all results and conclusions are made were generated using these methods.

3.2 Horizons

Nine horizons were interpreted: Base_1, Base_2, Base_3, Base_4, St. Peters Limestone, Hindsville Limestone, Basal Hale Sandstone, Orr Sandstone, and Sells Sandstone. The specified horizons were chosen for their regional consistency and the strong amplitude associated with their reflections.

Base_1, Base_2, Base_3, and Base_4 are the deepest reflectors and assumed to represent basement structures. The Precambrian basement is not exposed on the surface in Arkansas; however, there are basement penetrations by several wells distributed throughout

the state. One well is located near the study area and is used to tie the character of the basement reflectors (figure 3.1 & 3.2). This well is the Arco Exploration 1 Wayne L Edgmon, which penetrated diabase and granite (Denison, 1984). The lithologic descriptions from outcrop in northern and central Arkansas by McFarland (2004) for the rest of the interpreted horizons are listed below in chronologic order from oldest to youngest. The St. Peters Sandstone is medium- to fine-grained sandstone that has few minor shale, limestone, and dolostone beds of Middle Ordovician age. The Hindsville Limestone is crystalline, fossiliferous limestone of Late Mississippian age and sits unconformably on top of the older Boone Limestone and Moorefield Shale formations. While the nature of the Hindsville does vary across this part of the basin (pinches out to the east of the study area), the peak associated with the Hindsville formation is easily interpretable across the study area. The Hale Formation is broken into two members: the first member contains silty shale intervals interbedded with siltstone and thin beds of fine-grained sandstone; the second member contains crossbedded, limy sandstone or sandy limestone with lenses of highly fossiliferous and oolitic limestone. The Hale Formation overlays the Fayetteville formation and marks the Mississippian-Pennsylvanian boundary. The Atoka formation has many informally named units including the Orr Sandstone and Sells Sandstone. The Atoka is a sequence of marine, silty sandstones and shales. Both the Hale and Atoka are of early Pennsylvanian age (figure 2.3).

All of the nine horizons listed above were interpreted manually, versus using autopick, to ensure accurate placement of the horizon along the seismic reflector. There is too much uncertainty associated with allowing the software to autopick the horizons and it is also too common for the autopicker to jump between reflector cycles in seismic data of the quality associated with the survey over the study area. The shallowest four horizons consist of

sandstone and limestone encased in shale that are associated with a positive impedance contrast. The deepest four horizons are thought to be basement reflectors with only Base_4 tying to the synthetic; however, the strong repeated reflections below Base_4 are consistent enough to carry regionally. Eight of the horizons were picked using the peak fill mode. The St. Peters sandstone is encased in limestone and is associated with a negative impedance contrast; for this reason the St. Peters event is the only horizon picked on a zero crossing.

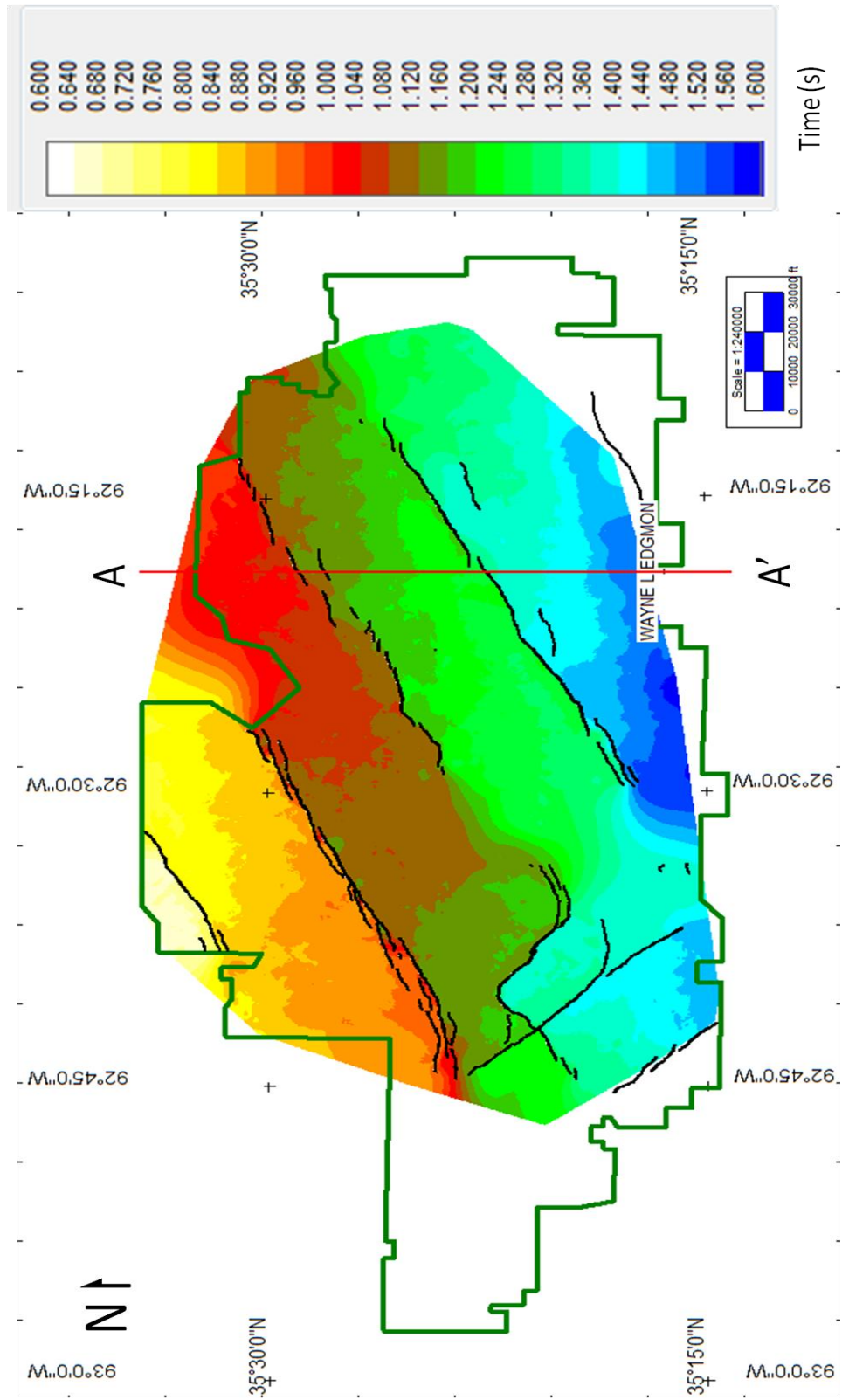


Figure 3.1: Base_4 time structure map with associated basement tie-in well Arco Exploration 1 Wayne L Edgemon. Black lines – basement fault polygons

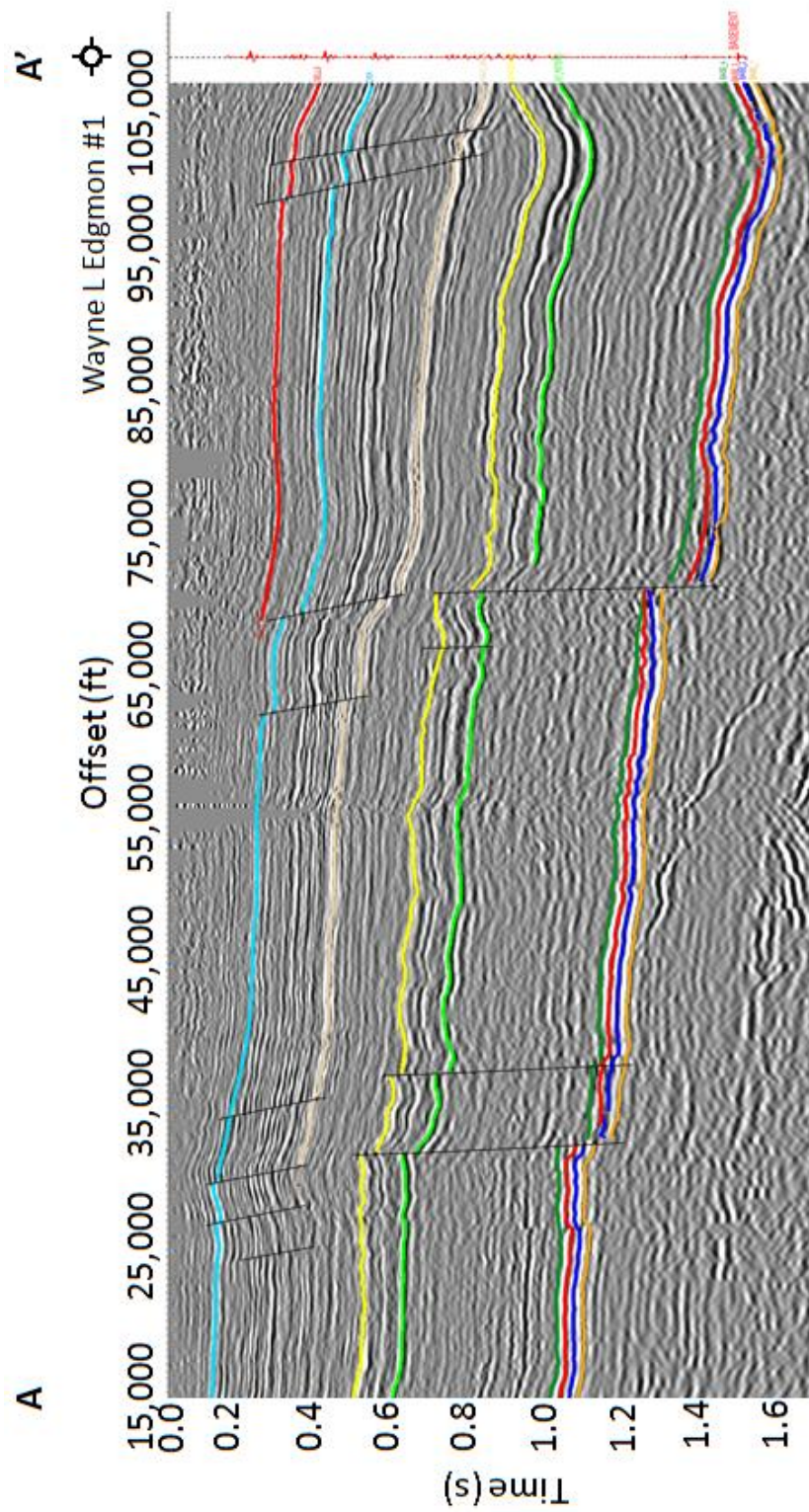


Figure 3.2: Cross-section A-A' indicating formation top, designated as basement, picked in well logs correlates to deep horizon reflectors. Black – deep and shallow faults; red – Sells, light blue – Orr; light brown – Basal Hale; yellow – Hindsville; light green – St. Peters; dark green, red, blue, and orange package of reflectors at depth – basement reflectors

3.3 Synthetic Ties and Manual Horizon Interpretation

Sonic logs measuring compressional velocity and density logs measuring bulk density were used within Kingdom's synthetic generation module (SynPAK) to generate reflection coefficient series. Wavelets used to convolve with the reflection coefficient series were generated by either estimating a Ricker wavelet or extracting a representative wavelet from the surrounding traces. Ricker wavelets were selected by calculating the dominant frequency ($F_{dom} = \frac{F_1 + F_2}{2}$) from the frequency spectrum of surrounding traces. Figure 3.2 illustrates a typical frequency spectrum calculated from the surrounding traces. The dominant frequency is calculated by averaging the maximum and minimum frequency from the frequency spectrum ($F_{dom} = \frac{10Hz + 95Hz}{2} = 52.5Hz$). Typical frequency spectra from the study area have a bimodal distribution with strong low frequencies around 40 Hz and strong high frequencies around 70 Hz. Minimum and maximum frequencies range from around 10 Hz to 95 Hz. Fifty-five Hz Ricker wavelets were predominately used. Extracted wavelets and higher frequency Ricker wavelets were used when the 55 Hz Ricker wavelet masked high frequency beds.

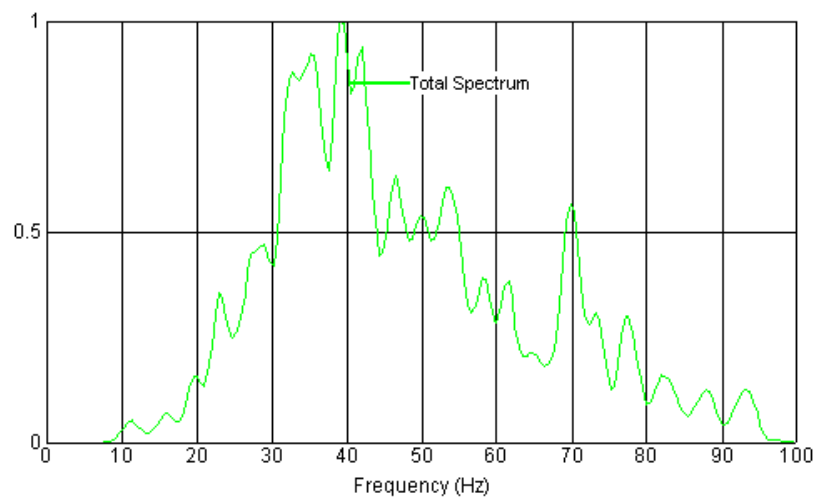


Figure 3.2: Frequency spectrum calculated in SynPAK for the Stobaugh, James 4-33PH28; typical spectrum for the study area.

Time-depth (T-D) charts were previously modeled from VSP and checkshot surveys and imported into Kingdom for a number of vertical pilot holes that were used to tie the time horizons to depth. This allowed for the accurate matching of amplitudes in time to specific geologic formation tops. Geologic formation tops, representing formal and informal units previously interpreted on well logs by regional geologists at SWN, were assigned to the T-D curves. Synthetic seismograms for each of the pilot wells were time shifted to match the Hindsville Limestone peak. Subsequent stretching and squeezing of the synthetics at shallower horizons followed in order to build a strong tie to the 3D volume (figure 3.3). After synthetic seismograms were generated for the study area, arbitrary seismic reflection lines were extracted in 2d/3dPAK between wells to generate cross-well horizon interpretations. From the cross-well grid, inlines and crosslines of reflection data were interpreted at decreasing intervals, starting with interpreting every 128th line and dividing the line spacing by two until every 4th line was interpreted. Figure 3.4 illustrates density of the manual interpretation for the Hindsville and is comparable to other horizons interpreted. Variations in synthetic seismograms across the field are shown in figures 3.5-3.12.

Stobaugh, James 09-15 #4-33PH28 Synthetic

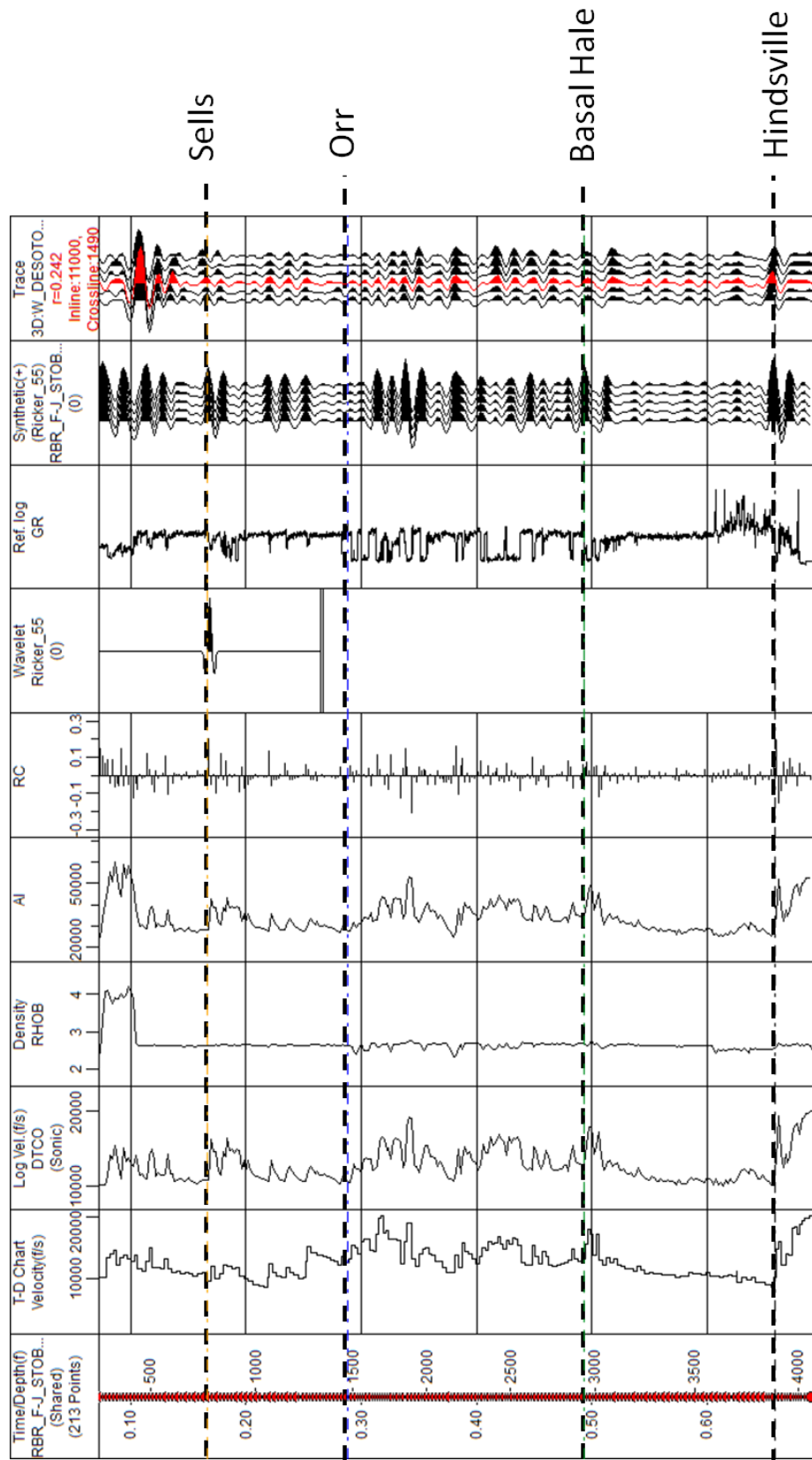


Figure 3.3: Synthetic seismogram for the Stobaugh, James 09-15 #4-33PH28 generated in SynPAK; typical synthetic seismogram for the study area showing strength of tie to the 3-D seismic volume.

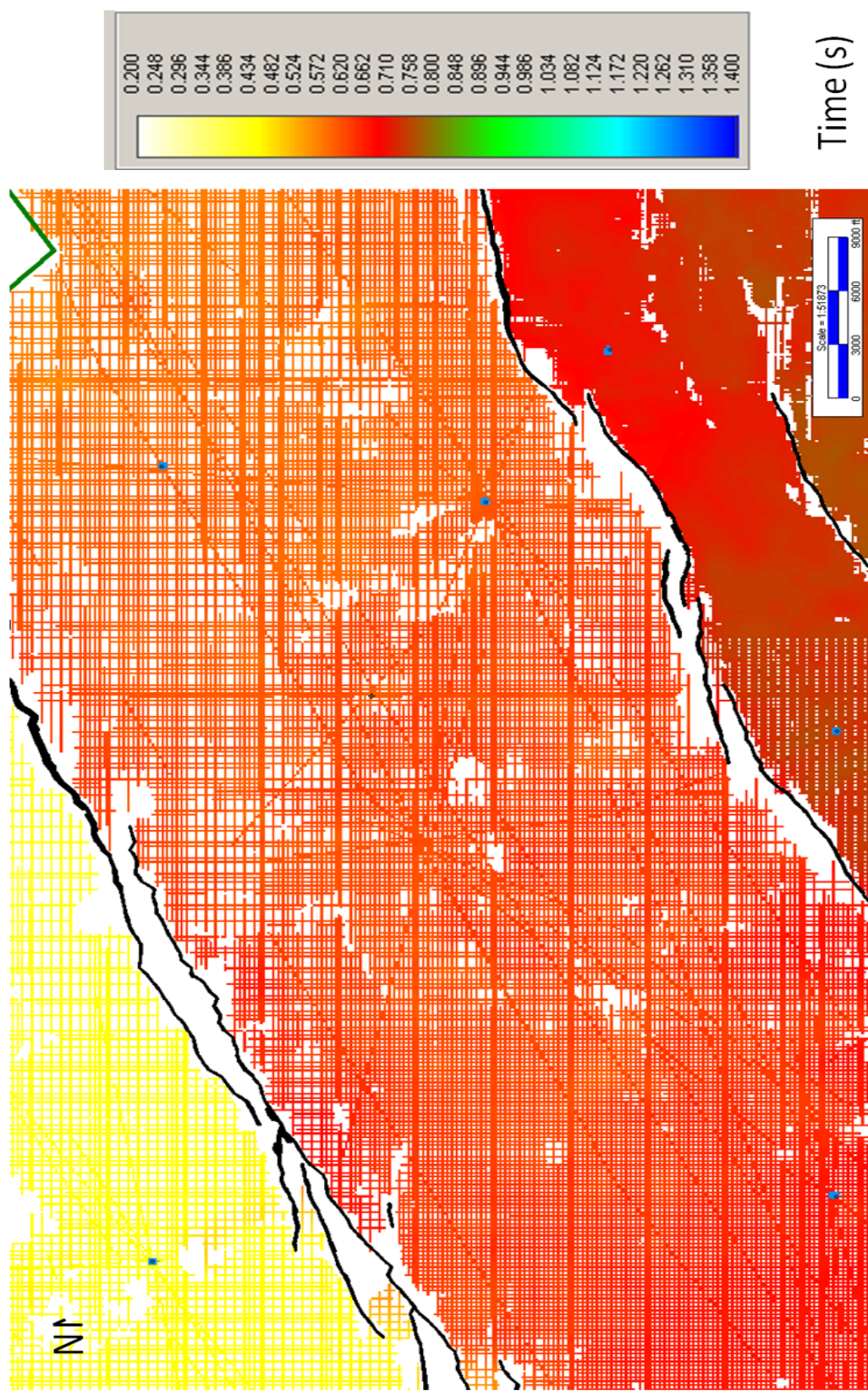


Figure 3.4: Generalized map showing seismic time interpretation density for the Hindsville time horizon. Interpretations were made between wells to generate strong ties to seismic and then extrapolated from those strong crosswell ties. At a minimum, each horizon was interpreted to every 4th line (approximately 440'). Black lines – fault polygons, blue squares – pilot wells for cross-well interpretations.

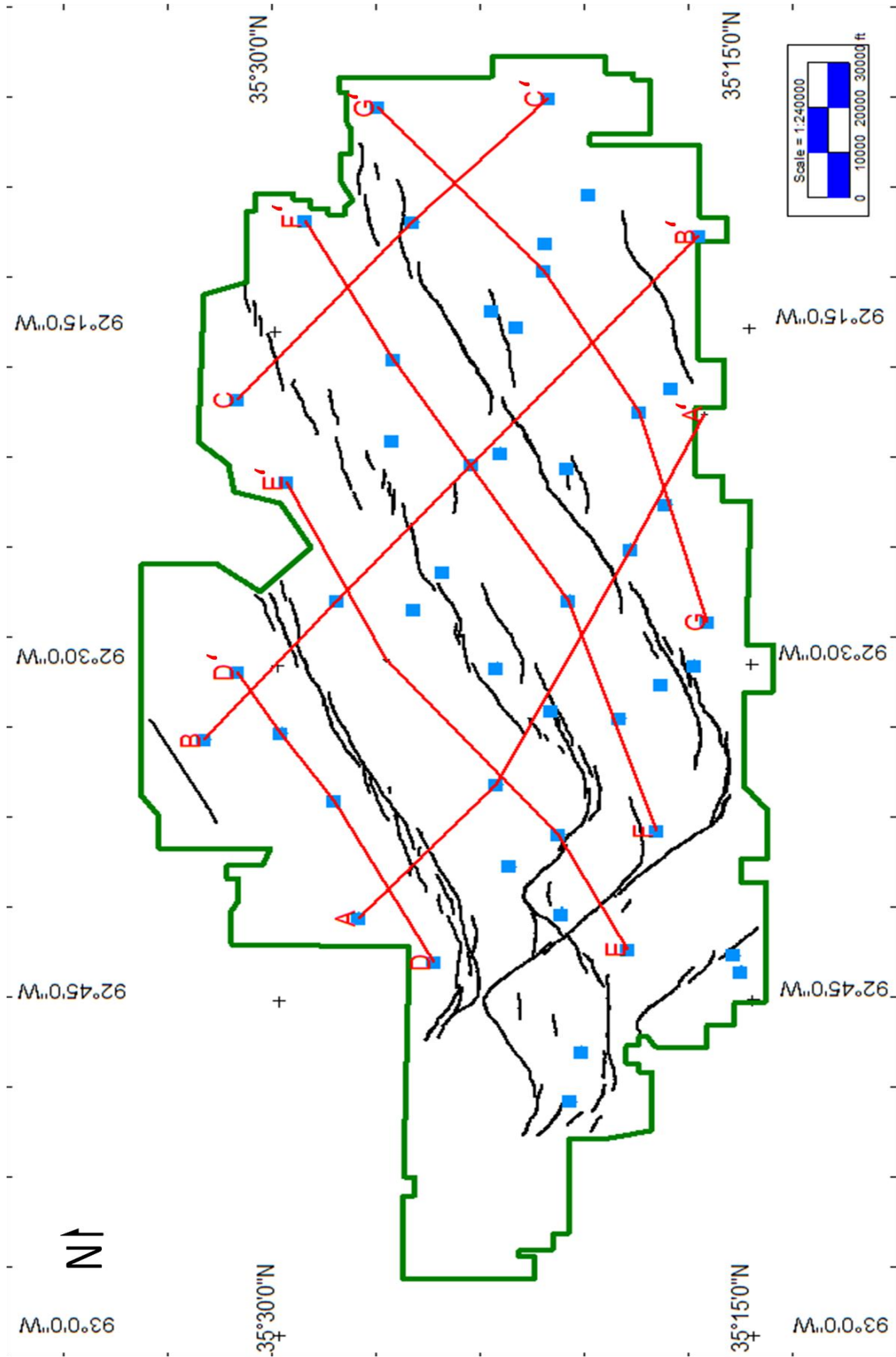


Figure 3.5: Study area with cross-section designations for figures 3.6-3.12. Blue squares – wells with synthetic seismograms; black lines – deep fault polygons.

GR – Gamma Ray (API)

Synthetic along depth track (Time & Amplitude)

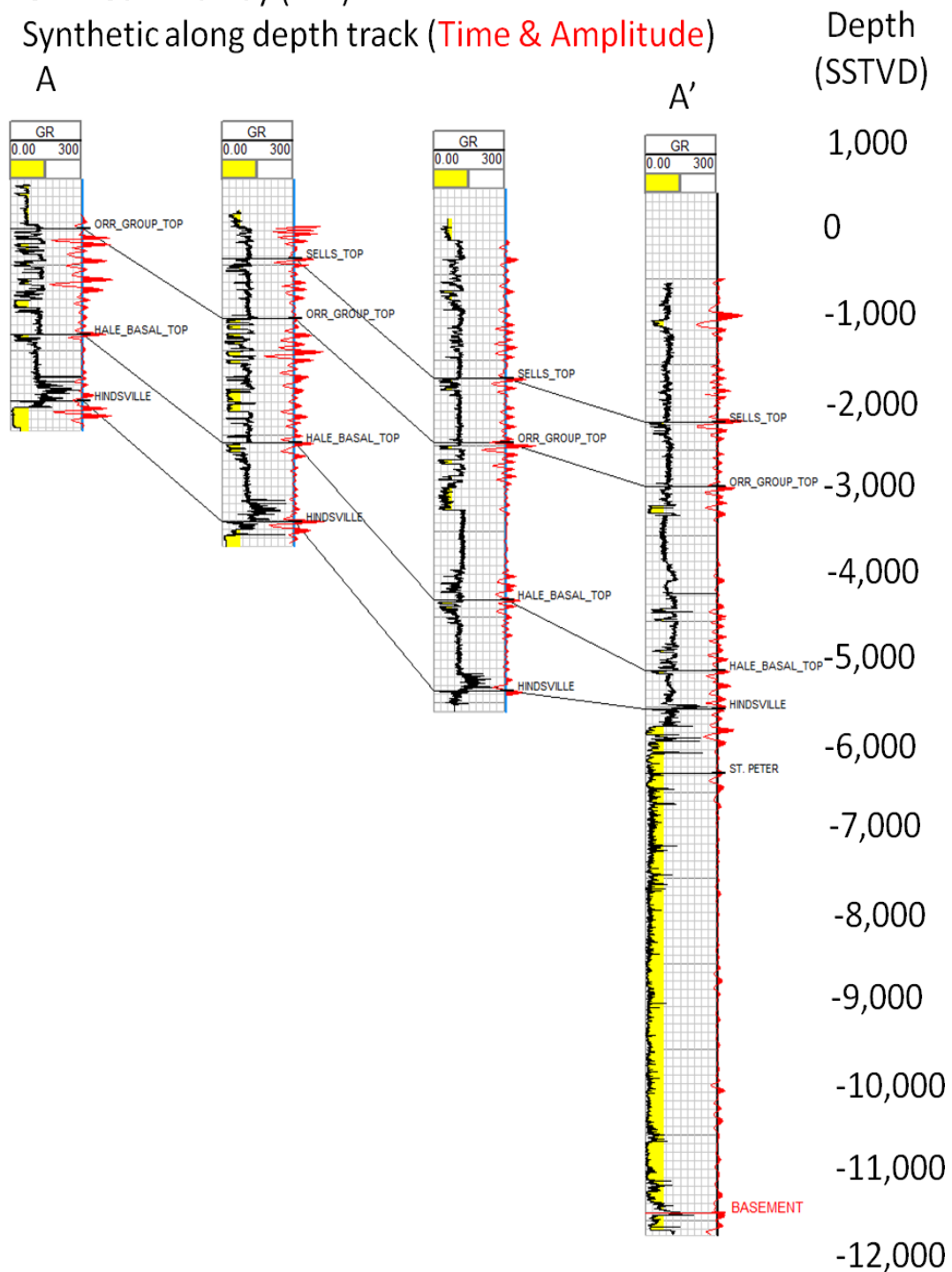


Figure 3.6: Cross-section A-A' showing general structure from gamma ray logs and variation in synthetics across the field. Yellow – indicates cold gamma ray reading or non-shale formation. Well names from left to right: Koone 09-16 #1-03PH, Stobaugh, James 09-15 #4-33PH28, Harris 08-13 #1-19PH, and Wayne L Edgmon #1.

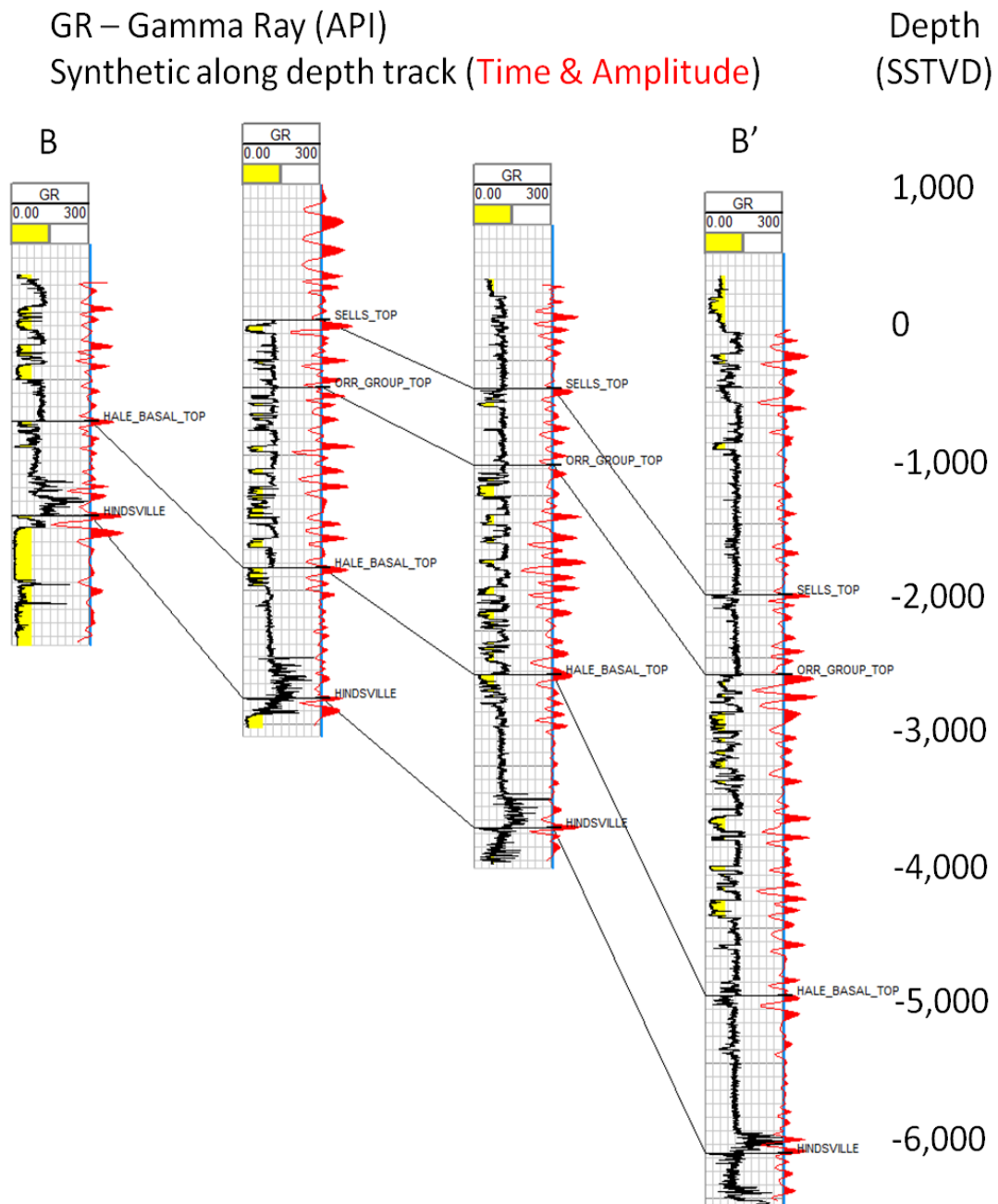


Figure 3.7: Cross-section B-B' showing general structure from gamma ray logs and variation in synthetics across the field. Yellow – indicates cold gamma ray reading or non-shale formation. Well names from left to right: Kidd 10-15 #2-02PH, Sisson 10-14 #3-35PH, Hutto 09-13 #1-23PH, and Brewer 08-11 #1-33PH.

GR – Gamma Ray (API)

Synthetic along depth track (Time & Amplitude)

Depth
(SSTVD)

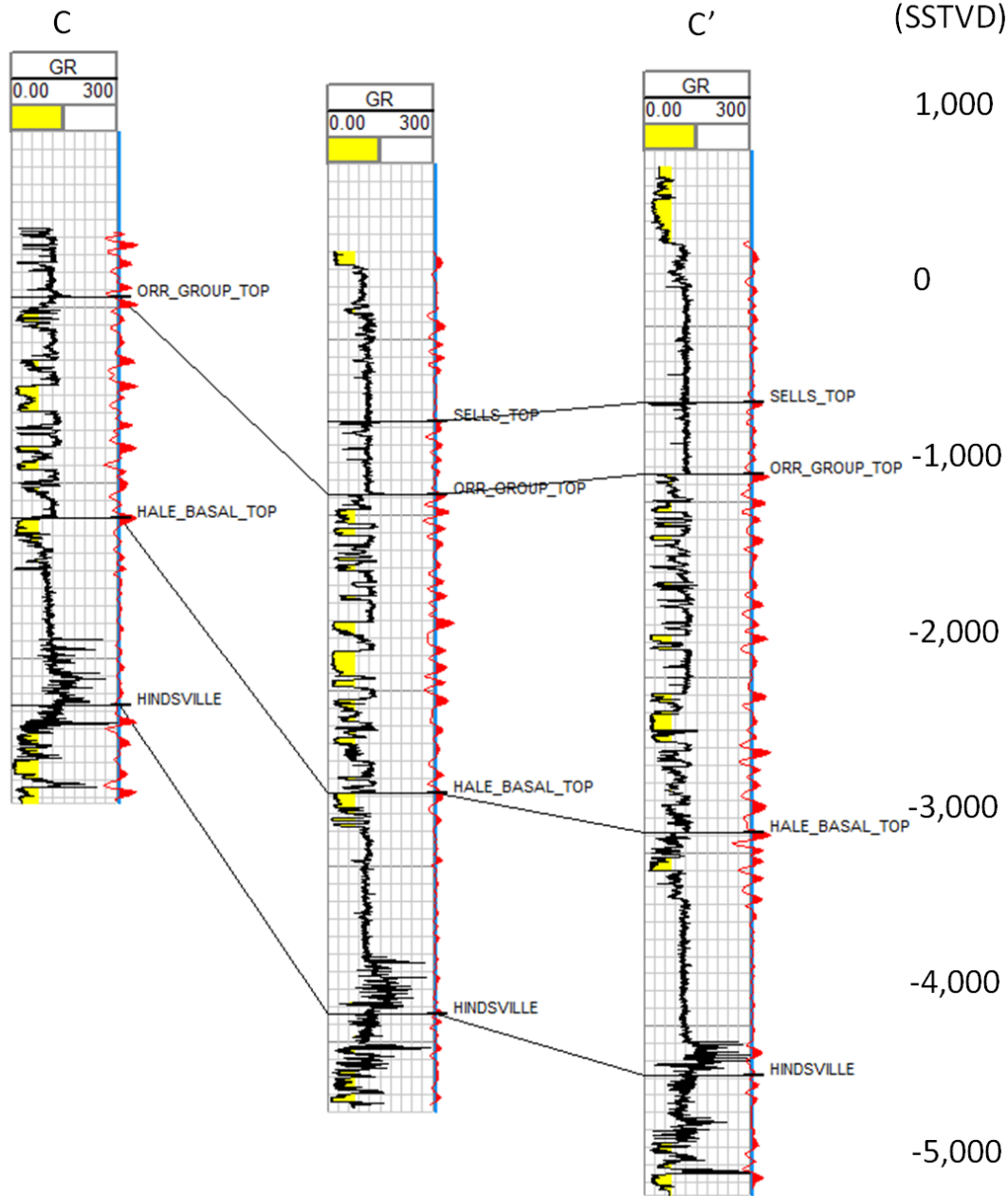


Figure 3.8: Cross-section C-C' showing general structure from gamma ray logs and variation in synthetics across the field. Yellow – indicates cold gamma ray reading or non-shale formation. Well names from left to right: Linn 10-12 #1-08PH, Edwards 09-11 #1-09PH, and Green Bay Packaging 08-10 #1-04PH.

GR – Gamma Ray (API)

Synthetic along depth track (Time & Amplitude)

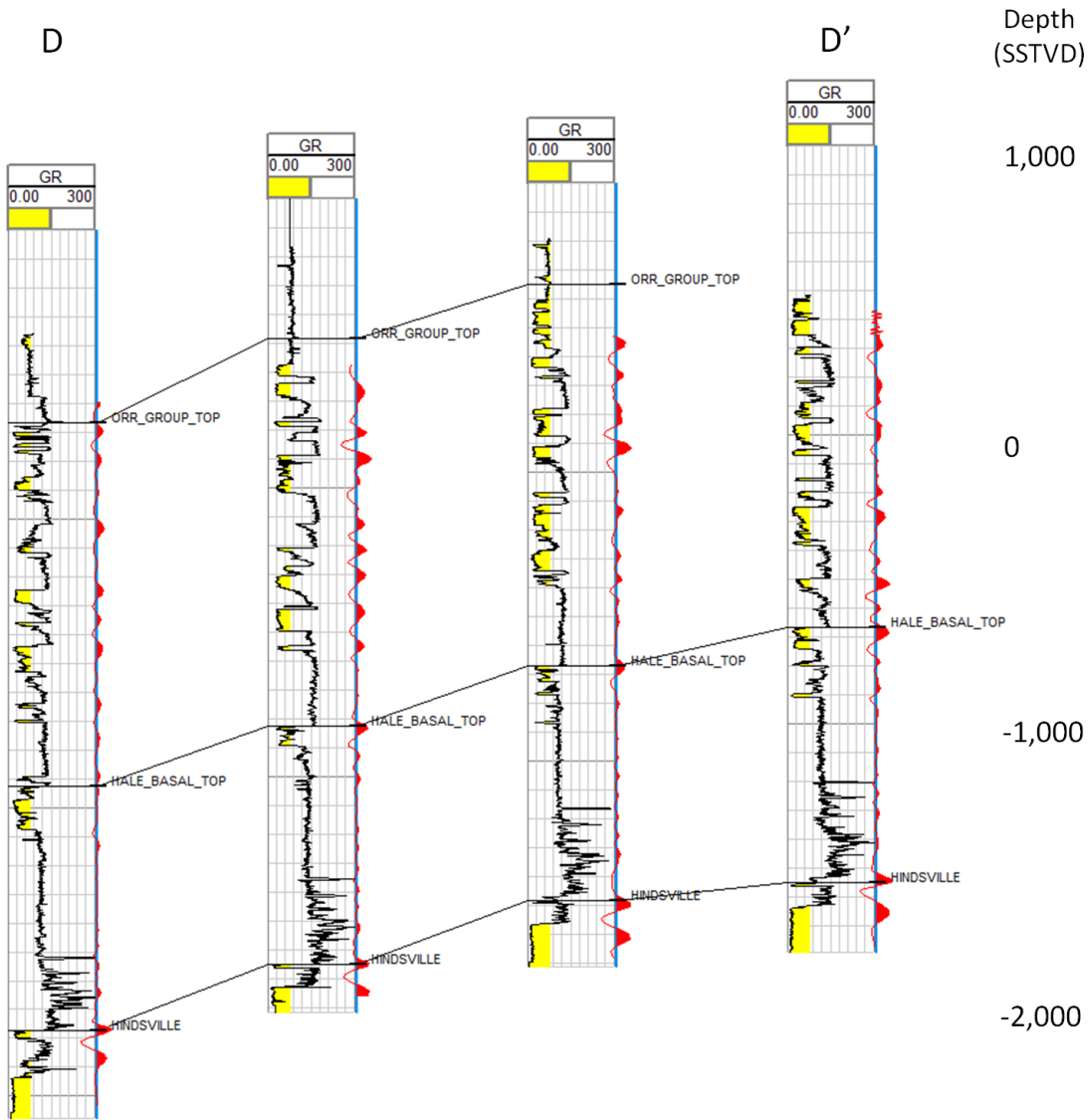


Figure 3.9: Cross-section D-D' showing general structure from gamma ray logs and variation in synthetics across the field. Yellow – indicates cold gamma ray reading or non-shale formation. Well names from left to right: Thompson 09-16 #4-17PH, Russell 10-15 #3-33PH21, Crowell 10-15 #4-23PH, and Mackey 10-14 #3-08PH.

GR – Gamma Ray (API)

Synthetic along depth track (Time & Amplitude)

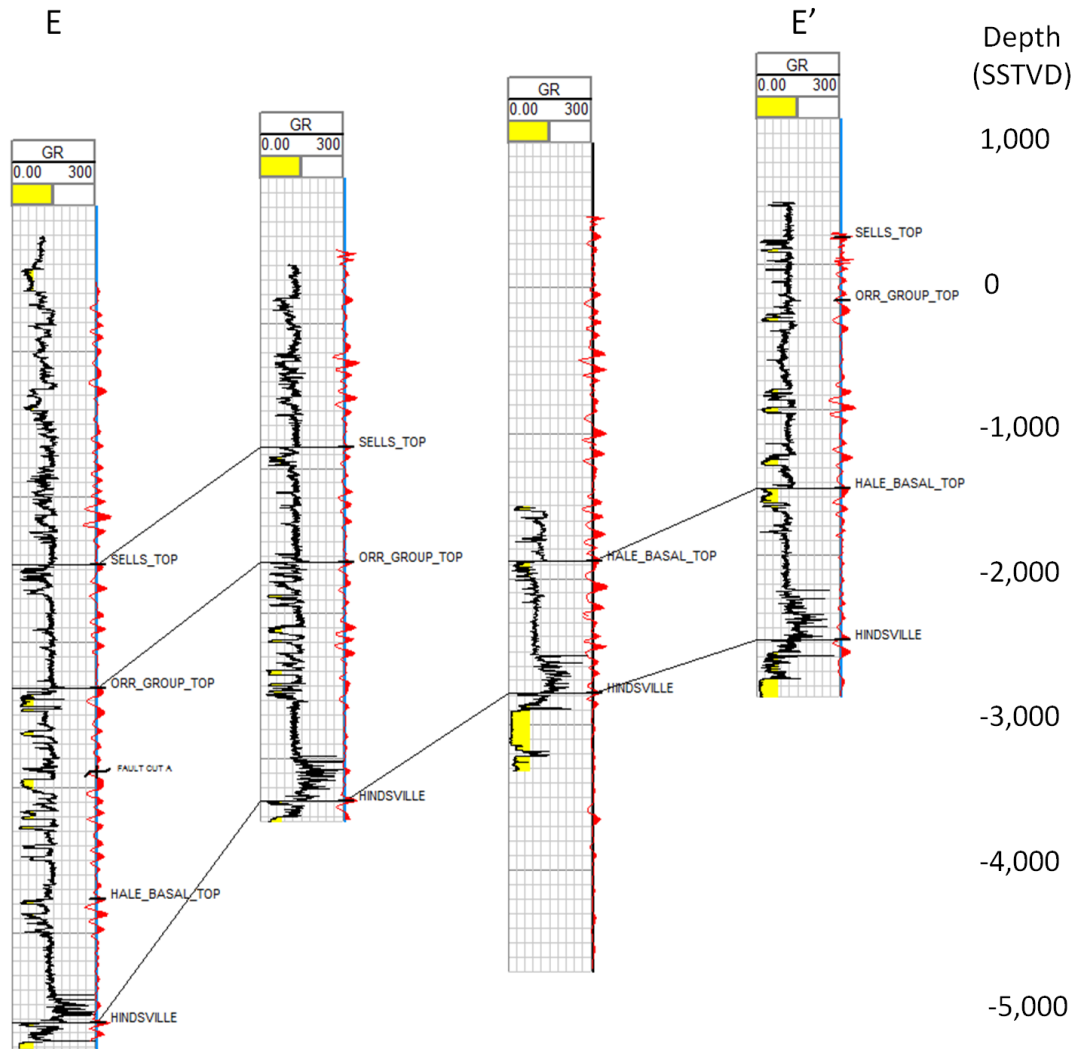


Figure 3.10: Cross-section E-E' showing general structure from gamma ray logs and variation in synthetics across the field. Yellow – indicates cold gamma ray reading or non-shale formation. Well names from left to right: Zimmerman, Antoinette 08-16 #1-21PH, McCoy, Kenneth 08-15 #2-07H6 ST1, Bryant 09-14 #1-4, and Hall, Darrell 10-13 #2-22PH.

GR – Gamma Ray (API)
 Synthetic along depth track (Time & Amplitude)

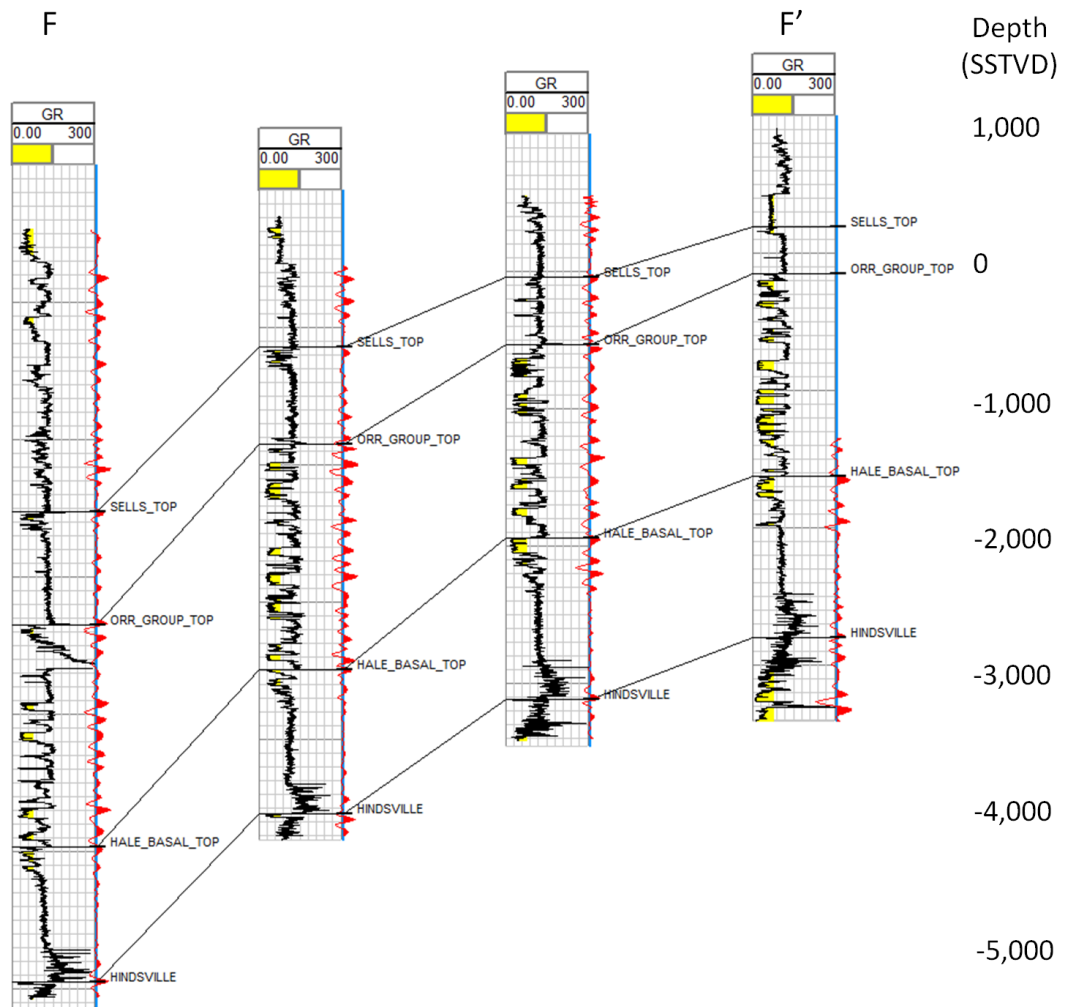


Figure 3.11: Cross-section F-F' showing general structure from gamma ray logs and variation in synthetics across the field. Yellow – indicates cold gamma ray reading or non-shale formation. Well names from left to right: Taylor 08-15 #1-29PH ST1, Harrison R 08-14 #1-11PH, Sneed 09-12 #2-04PH, and Green Bay Packaging 10-11 #1-21PH.

GR – Gamma Ray (API)

Synthetic along depth track (Time & Amplitude)

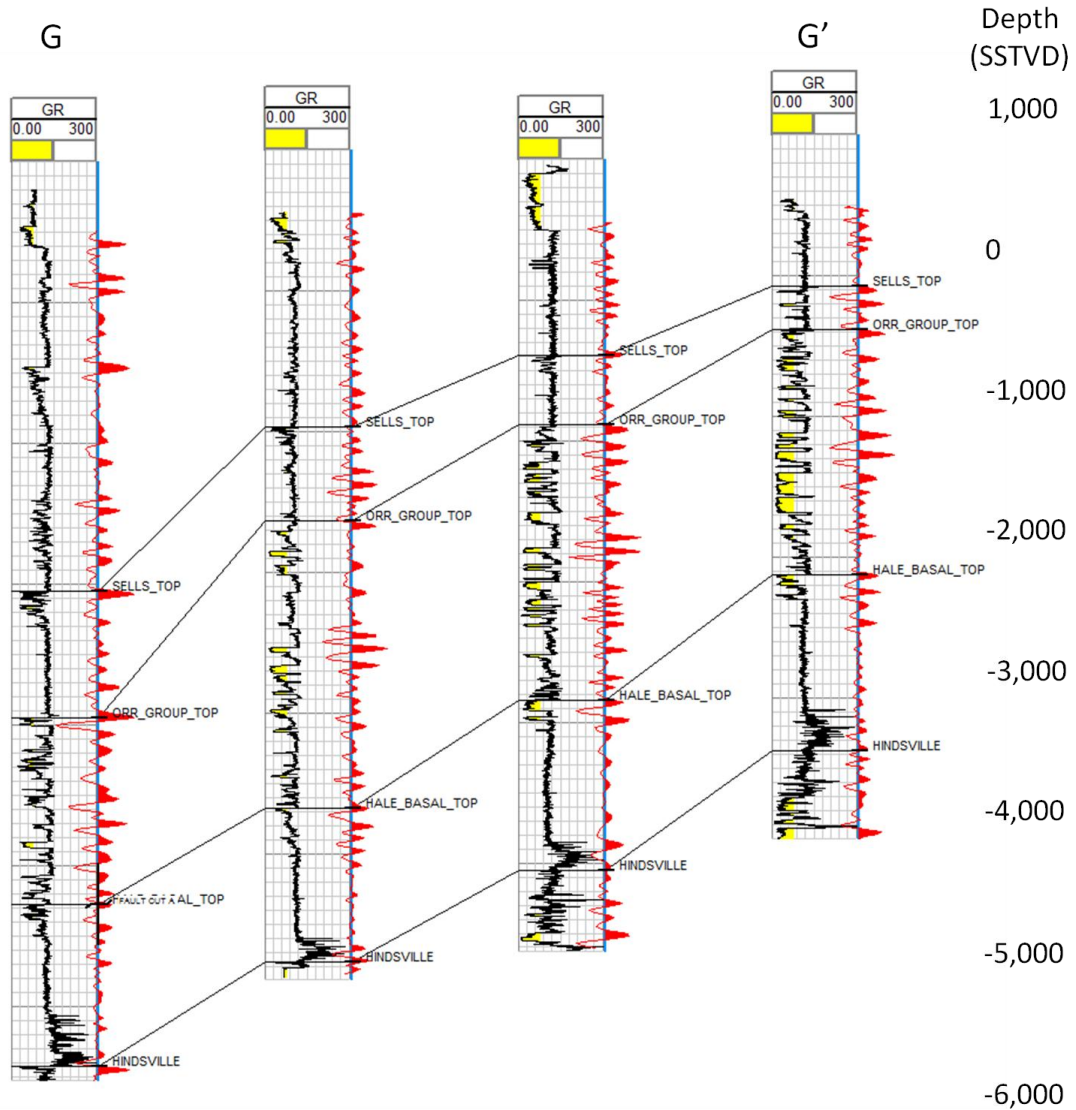


Figure 3.12: Cross-section G-G' showing general structure from gamma ray logs and variation in synthetics across the field. Yellow – indicates cold gamma ray reading or non-shale formation. Well names from left to right: Krisell Trust 07-14 #1-03PH, Kincaid 08-12 #1-19PH18, Sneed 08-11 #1-06PH, and Pearce 09-10 #1-05PH.

It is important to note that the formation tops used for depth conversion were delineated using density porosity logs. The tops were picked in such a manner that more emphasis was put on the stratigraphic significance rather than on the mechanical significance of the top. Because the tops were not picked on mechanical boundaries that would produce strong impedance changes, the formation tops have some separation between the picked position and the shale, sandstone, and limestone interfaces seen on the gamma logs.

3.4 Fault Interpretation

Faults were picked in cross-section view while interpreting time horizons. Many iterations alternating between inlines and crosslines were made using the PSTM reflection volume in order to spatially constrain faulting. Further constraints were made by incorporating horizon extracts from post-stack seismic attribute volumes such as coherence and ant track. Coherence volumes calculate a trace-to-trace variability within a particular sampling interval, thereby indicating lateral discontinuities (figure 3.13). Ant tracking is a filtering algorithm in Schlumberger's Petrel ge modeling software that further highlights linear discontinuities from a preexisting seismic attribute volume; in this case coherence (figure 3.14). Both extractions were used as supplemental information to help guide position of manually interpreted faults. It is important to note that not all high amplitude events in figures 3.13 & 3.14 are interpreted to be associated with faults; however, all faults interpreted in this study have associated nearby high amplitude events. Fault polygons were then generated for map displays and contouring purposes using Kingdom's auto fault polygon generator using the default settings. The auto generator was deemed sufficient for generating fault polygons because there is high confidence in the time horizon interpretations and little room for error since the faults are at high angles. This prohibits the function from generating large block polygons.

Fault analysis was completed using Kingdom, Microsoft Excel, and Midland Valley 2D Move. Throw for each assigned fault segment was calculated by subtracting depth structure of the hanging wall from the corresponding structure of the footwall. Depths on the hanging wall and footwall were determined from map view at the center of each fault segment where maximum displacement tends to be (Twiss and Moores, 2007). Fault lengths were determined by exporting the generated fault polygons from Kingdom into Excel, where it is relatively straight forward to determine the distance between each node in every fault polygon. The length and azimuth for each fault polygon was estimated using the two fault polygon nodes that are the furthest apart. For most faults in the study area, the before mentioned workflow is sufficient to give accurate lengths and azimuths for reasonably straight faults. However, there are some faults in the study area that have 90° bends and have skewed fault lengths and azimuths. The skewed fault lengths and azimuths do not have enough error to be deemed unreliable for general qualitative fault orientation analysis. Fault lengths and azimuths were then imported into 2D Move as structural dip data. The azimuth of the fault was designated as strike and the orientation analysis function was used to generate rose diagrams.

Trace-to-trace
variability
(amplitude)

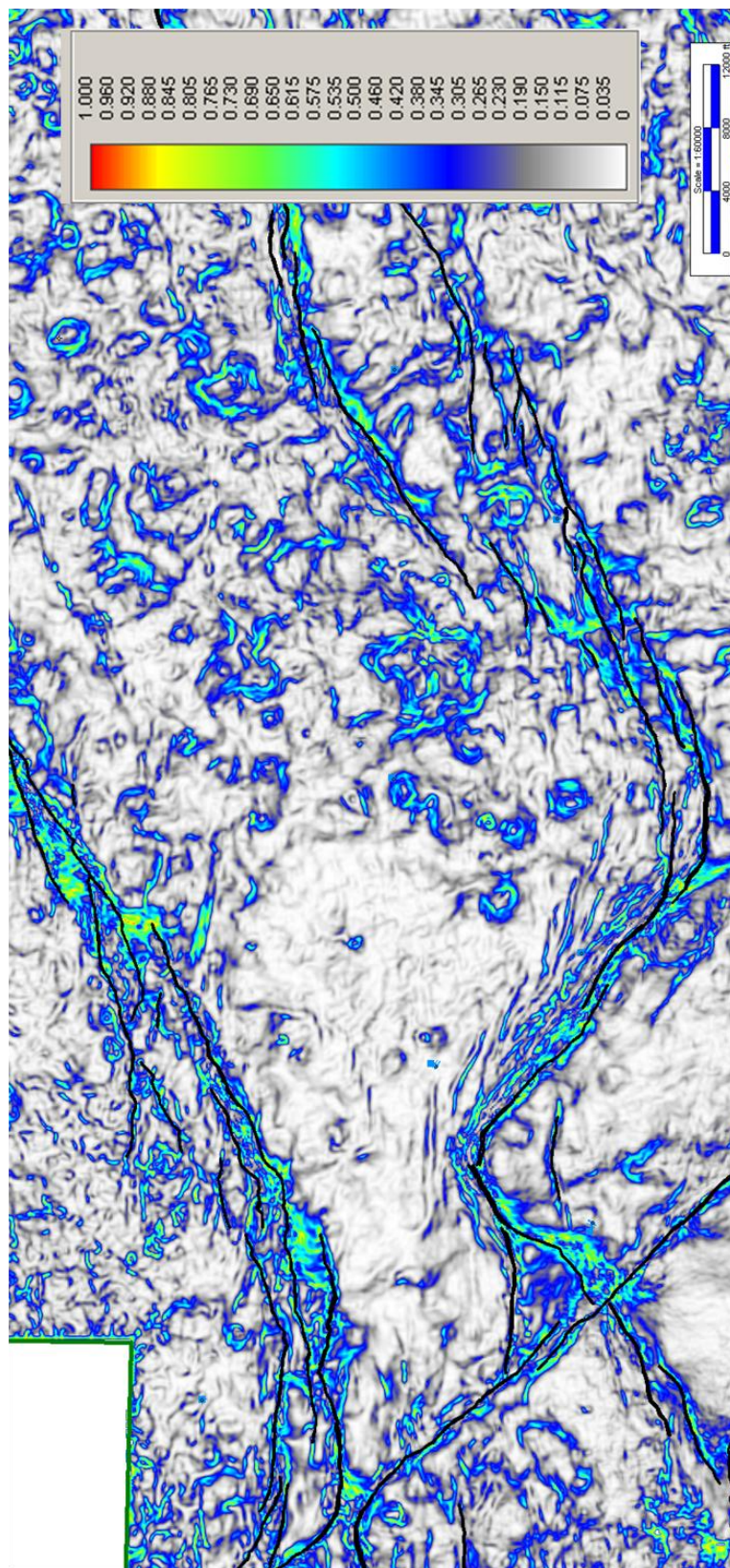


Figure 3.13: Coherence extraction from the Hindsville time horizon. Black lines indicate interpreted faults that intersect the Hindsville time horizon and color represents the magnitude of trace-to-trace variability.

Continuity of
Trace -to-trace
variability
(amplitude)

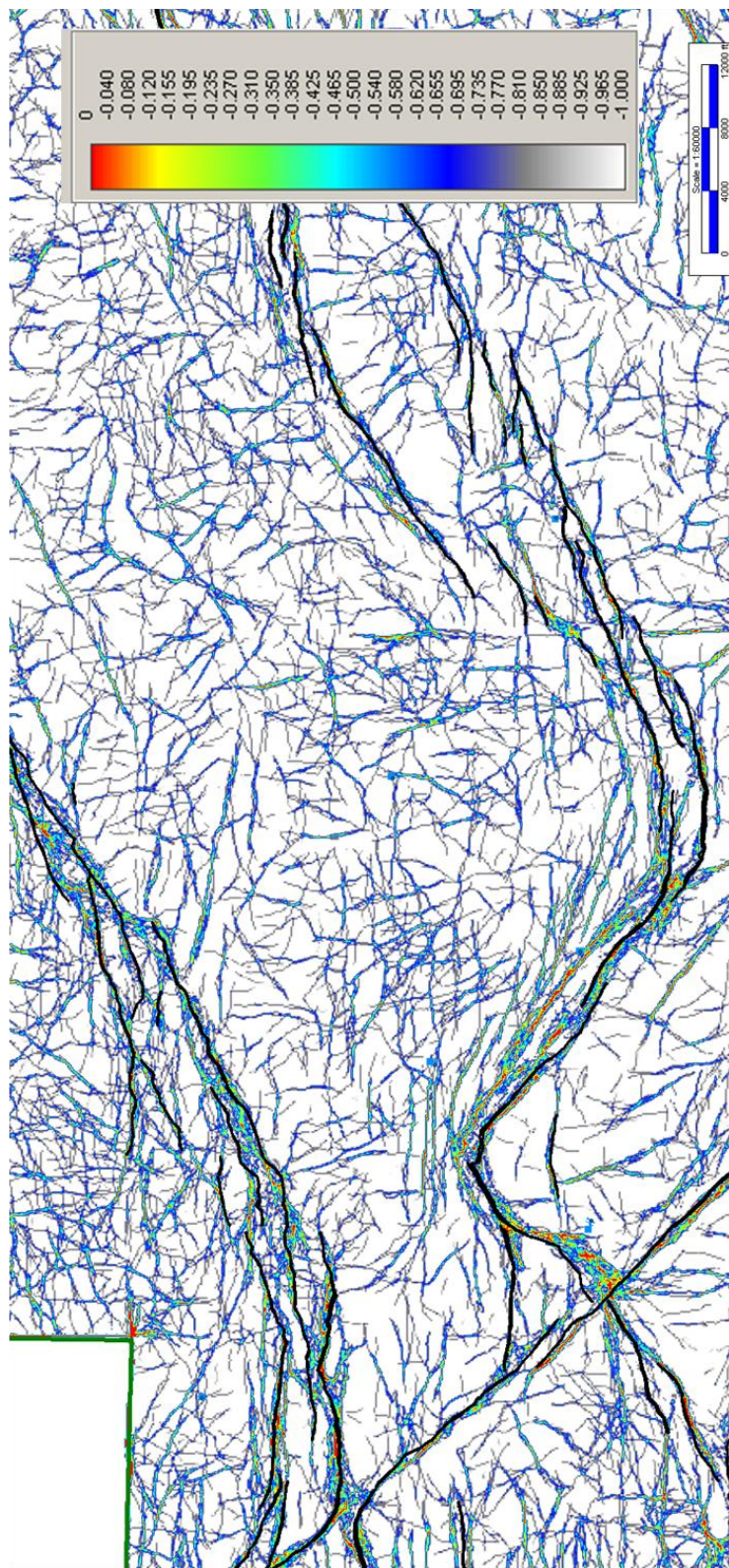


Figure 3.14: Ant track extraction from Hindsville horizon. Black lines indicate interpreted faults and color indicates the amplitude of the continuity of trace-to-trace variability.

3.5 Gridding and Depth Modeling

Manually interpreted time horizons (spaced every 4th inline and crossline) were generated within 2d/3dPAK using a simple Flex Gridding algorithm. The flex gridding parameters were set to minimum curvature (0) and midway smoothness (6). Grid cell sizes were set to 110 ft (33.5 m), matching the seismic survey bin spacing. The 110 ft (33.5m) bin spacing also removes the effect of any cell averaging, leaving only 1 datum per cell. The automatically generated fault polygons were incorporated into the gridding function.

The depth control from formation tops picked in wells also were gridded using a flex gridding algorithm so that accurate depth models could be generated for each of the time horizons. These formation tops were interpreted by geologists at SWN and then were gridded using minimum tension (1) and the default smoothness (4) for the gridding parameters. Minimum tension was used to prevent the grid from shifting the picked formation tops up or down from their actual position. Grid cell sizes were set to the same location and size as the time grids mentioned above to minimize the differences between the time and depth grids within the model. A limit on distance from control points were set to half the cell size at 55 ft (16.75 m). This creates a grid which only has values at locations where formation tops have been interpreted and prohibits the algorithm from interpolating between wells; therefore generating a set of accurate depth control points.

Velocity control points were generated by dividing the time grid by the depth control points using the extended math calculator. Velocity control points were then gridded using the flex gridding algorithm with minimum curvature (0) and midway smoothness (6) using the same grid size (110 ft or 33.5 m) and location as that used for the time and depth grids above. The average velocity grid was interpolated using the automatically generated fault polygons.

The final depth structure maps were generated by multiplying the final average velocity by the original time grid of the geologic horizon. The final depth structure maps are in sub-sea total vertical depth (SSTVD).

Depth models for horizons deeper than Base_4 were not completed due to the lack of well penetrations at these depths. The Sells, Orr, Basal Hale, Hindsville, and St. Peters formations were all modeled in depth using the average velocities. There is high confidence in these depth structure maps because of the large number of formation tops from well penetrations present in the study area (737 wells for the Sells, 893 wells for the Orr, 877 wells for the Basal Hale, 298 wells for the Hindsville and 20 wells for the St. Peters.)

The summary for basic workflow to model sub-sea depth structure maps is as follows:

1. Grid Time from horizons
2. Grid tops from formation (d_{cntrl})
3. Calculate velocity control ($V_{cntrl} = (-2) * d_{cntrl} / \text{time grid}$)
4. Grid velocity map using same parameters as time grid (V_{grid})
5. Calculate depth model ($\text{Depth} = V_{grid} * \text{time grid} / (-2)$)

Multiplying and Dividing by (-2) in steps 3 and 5 are not necessarily needed; however, step 3 is a way to determine a positive average velocity down to formations from the surface. Step 5 readjusts the depth back to SSTVD.

The assumed top of Basement (as reflected by the Base_4 horizon) was modeled in depth using an interval velocity below the St. Peters Limestone. An interval velocity was used because there is only one well in the study area that penetrates basement. The Wayne L Edgmon #1 penetrates the St. Peters at -6,284 ft (-1915 m) SSTVD and Base_4 at -11,430 ft (-3484 m) SSTVD, giving a thickness of 5,146 ft (1569 m). Using the time thickness from the

nearest trace of 0.423s, an average velocity was estimated to be ~12,165 ft/sec (3708 m/sec). The average velocity was then multiplied by the Base_4 to St. Peters isochron to determine the Base_4 to St. Peters isochore. The Base_4 to St. Peters isochore was then added to the St. Peters depth structure map in order to determine the Base_4 depth structure map.

3.6 Isochores

Both Isochron and isochore maps were generated using the extended math calculator in Kingdom. Isochore maps were primarily used to assist with structural interpretation and were generated by subtracting the shallower formation structure from the corresponding deep structure formation. Fault polygon sets were used to indicate approximate position of faults within the designated isochore intervals. Fault polygons were included in the isochore maps to indicate areas that see thinning or thickening across faults. The St. Peters fault polygons were used in the deep regime and the Orr fault polygons were used in the shallow regime. In the transition zone (Hindsville – Basal Hale) both sets were used for interpretation.

4 Interpretation and Results

4.1 Structural Geology

The structure for the study area can be divided into two separate regimes, a deep regime and a shallow regime. The sectioning of the structure is similar to Van Arsdale and Schweig's (1990) description for the Arkoma Foreland. Each regime is described from a 3D interpretation and then linked in the following section. Relative timing and structural modeling are presented as well.

4.1.1 Deep Structure

The St. Peters Sandstone sub-sea depth structure maps in figure 4.1 illustrate the deep structural regime. The deep structure is characterized by NE/SW-trending down-to-the-southeast normal faults and NW/SE-trending down-to-the-southwest normal and strike-slip faults. The eastern portion of the structure predominately trends NE/SW creating a system of terraces that deepen to the south and east. Further west, three faults are oriented NW/SE, with structure deepening to the south and west. Faults bounded by the three large NW/SE faults return to NE/SW trends over a short distance before bending to an E/W orientation. The exact orientation distribution of the 88 interpreted faults in the deep structure is illustrated in figure 4.2. Fault azimuths for the St. Peters have a bimodal distribution. The deep faults terminate up-section from the Hindsville reflector but deeper than the Basal Hale sand reflector (figure 4.3). Seismic resolution is too low in the Morrowan Shale to determine exact termination of the deep faults; however, the Morrow exhibits thickening of the hanging wall and thinning of the footwall (figure 4.4). As a result, the Morrow is draped over the deep faults creating a monocline. Amount of thinning in the footwall block is exaggerated in figure 4.3 & 4.4 due to velocity pull-up. Amount of thickening has been confirmed from well logs in the footwall blocks. Deep faults penetrate the basement reflectors and extend past seismic resolution at depth. The exact depth of fault termination is unknown. Fault length and displacement are quite large for the deep structure. The graphs in figures 4.5 and 4.6 show log-log plots of fault length versus normal displacement for the deep faults. The graphs follow the general rule of thumb that as fault length increases fault displacement also increases. The NE/SW-trending terrace fault traces 2, 4, and 6 have the largest displacements among the fault trends, with maximum displacements of 1600 ft (488 m), 1600 ft (488 m), & 1350 ft (411 m) respectively. The NW/SE-trending faults A, B,

and C, have a maximum displacement of 850 ft (259 m), 1075ft (328 m), and 1325 ft (404 m) respectively. Even with the noted amount of displacement, the faults are not continuous across the field. Each fault is soft-linked with a steeply dipping relay ramp (figure 4.7). The relay ramps seen in the deep structure tend to be different than those described by Larsen (1988) in that there is no interpreted detachment at depth; moreover the deep faults formed between two separated planar normal faults, much like ones described in Peacock and Sanderson (1991). The relay ramps interpreted in the study area can be defined as synthetic overlapping transfer zones (Morley et al., 1990). While most relay ramps in the area cover only a small aerial extent, the ramp present along the central terrace fault (#3) is large in comparison (figure 4.8). Figure 4.9 illustrates a possible structural high below the large relay ramp along the central fault terrace. Both sets of relay ramps are observed in the interaction stage, which is where the tilt of bedding between two faults or deflection of strike of one or both faults towards the ramp occurs (Hus et al., 2005). Previously only dip-slip motion has been considered for the deep faults. However, the bending of the deep faults from NE/SW to NW/SE has implications for a large amount of strike slip displacement. An isochore map of the St. Peters to the Hindsville also indicates strike-slip motion along fault A (figure 4.10).

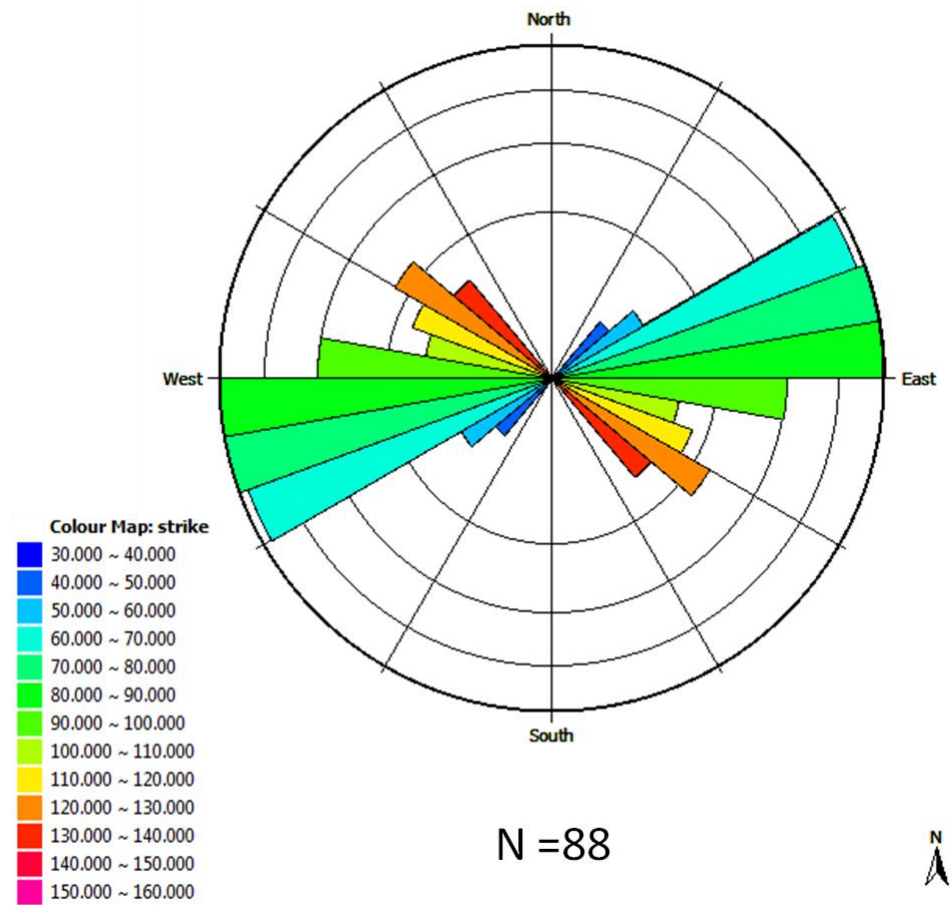


Figure 4.2: Deep fault azimuth rose diagram (bidirectional); 88 faults interpreted to penetrate the St. Peters Limestone. Different colored 10° intervals are used to emphasize the bimodal distribution of the prominent NE/SW trend and NW/SE trend of the deep faults.

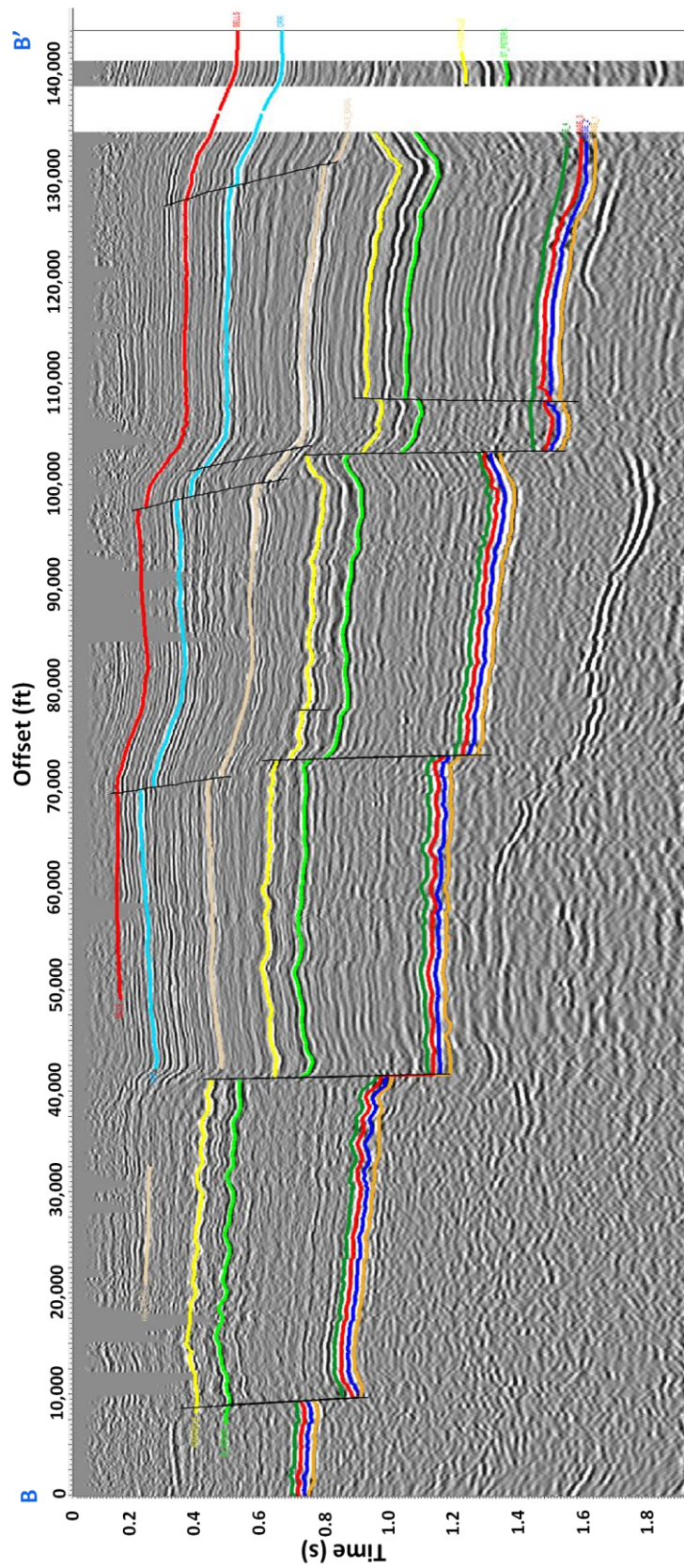


Figure 4.3: Arbitrary dip line from the pre-stack time migrated volume; black – deep and shallow faults; red – Sells, light blue – Orr; light brown – Basal Hale; yellow – Hindsville; light green – St. Peters; dark green, red, blue, and orange package of reflectors at depth – basement reflectors.

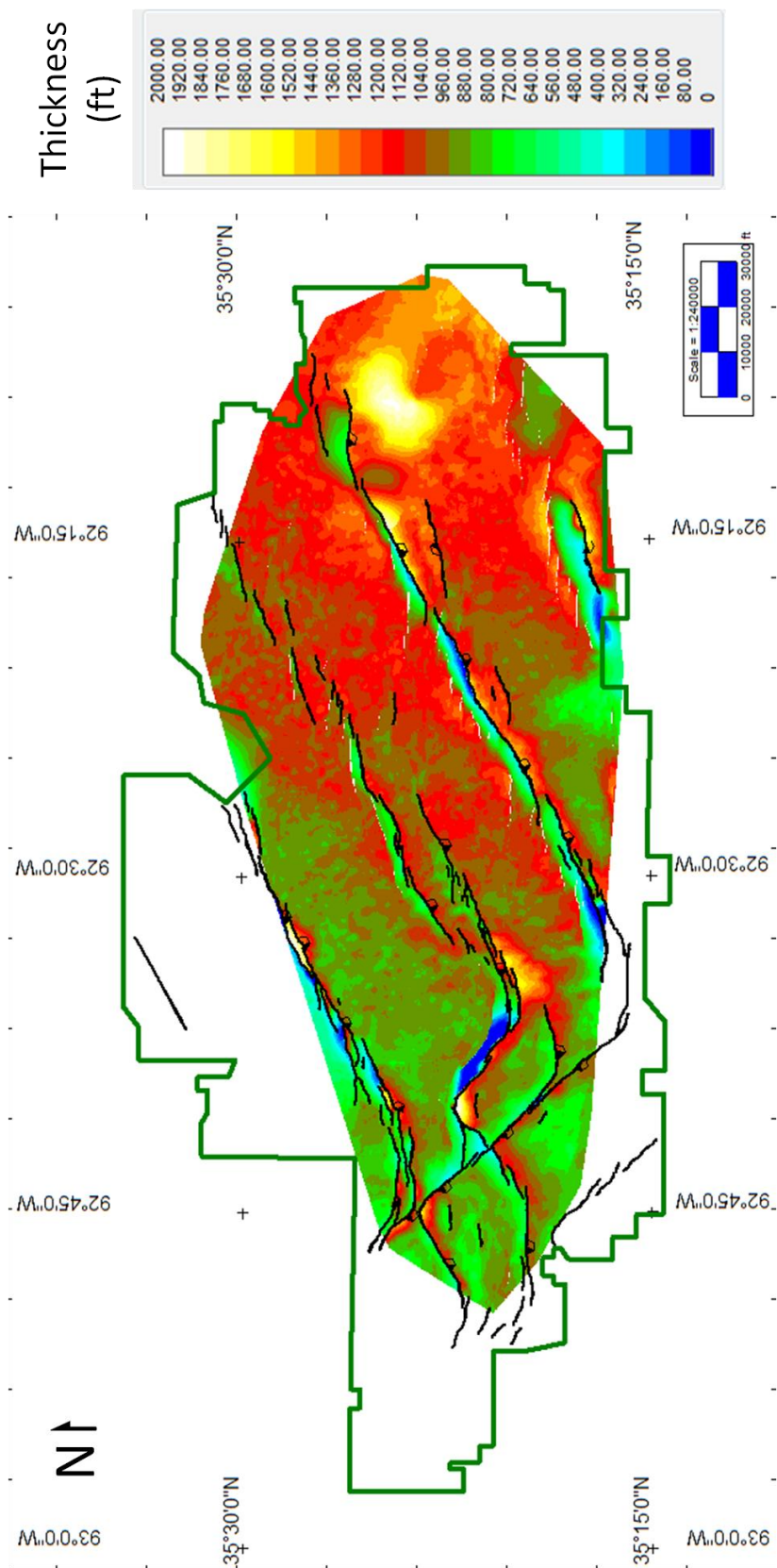


Figure 4.4: Hindsville – Basal Hale isochore map; generally indicates zone is thicker in the east and thinner in the west; indicates thinning of footwall block and thickening of hanging wall block. Black lines – deep faults.

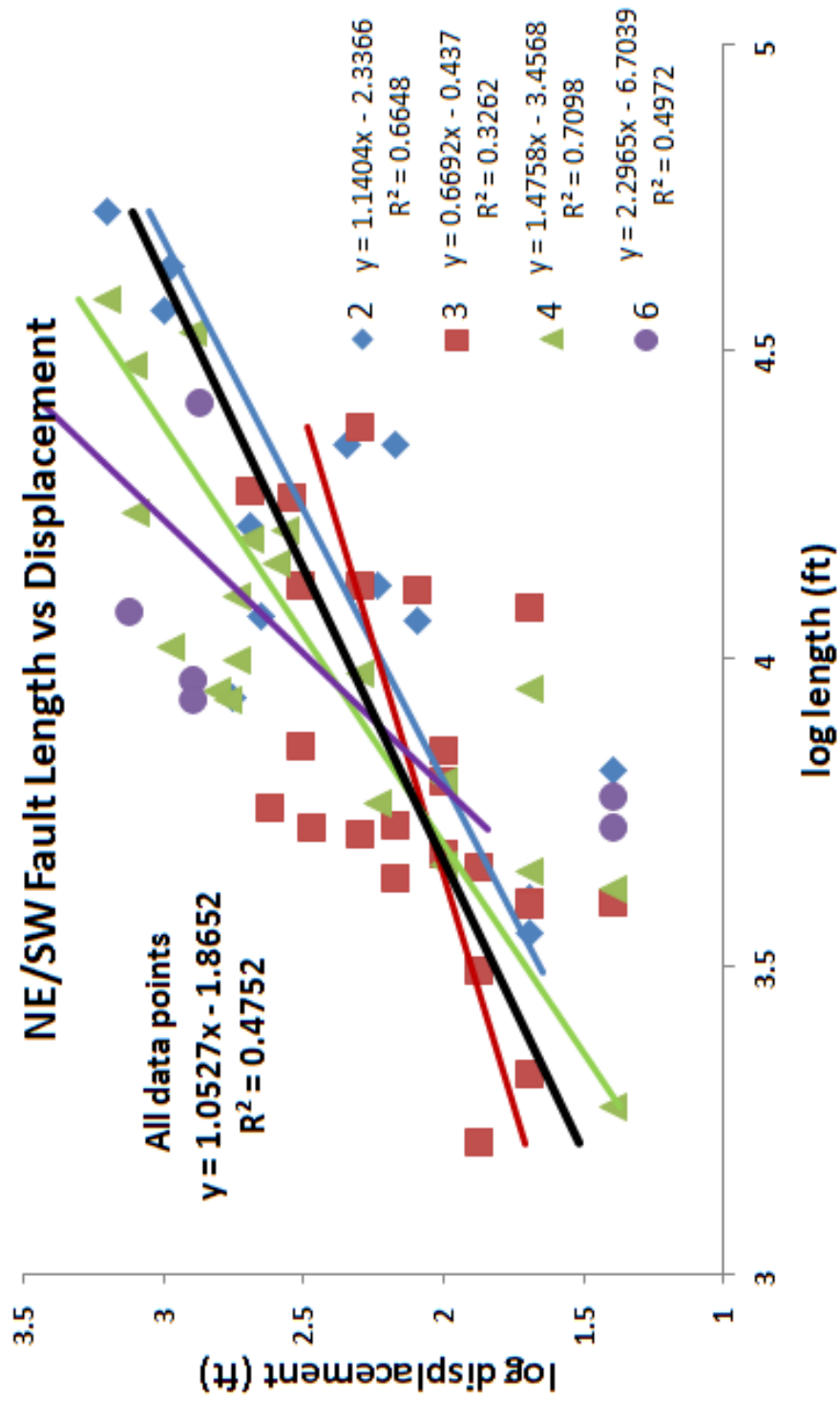


Figure 4.5: Log-log plot of fault length vs. displacement (dip-slip) for the deep NE/SW-trending faults; fault labels correspond to those in figure 4.1. Trendlines included for each fault set (color lines correspond to color of data symbols); black trendline represents all data points including points from faults A, B, & C.

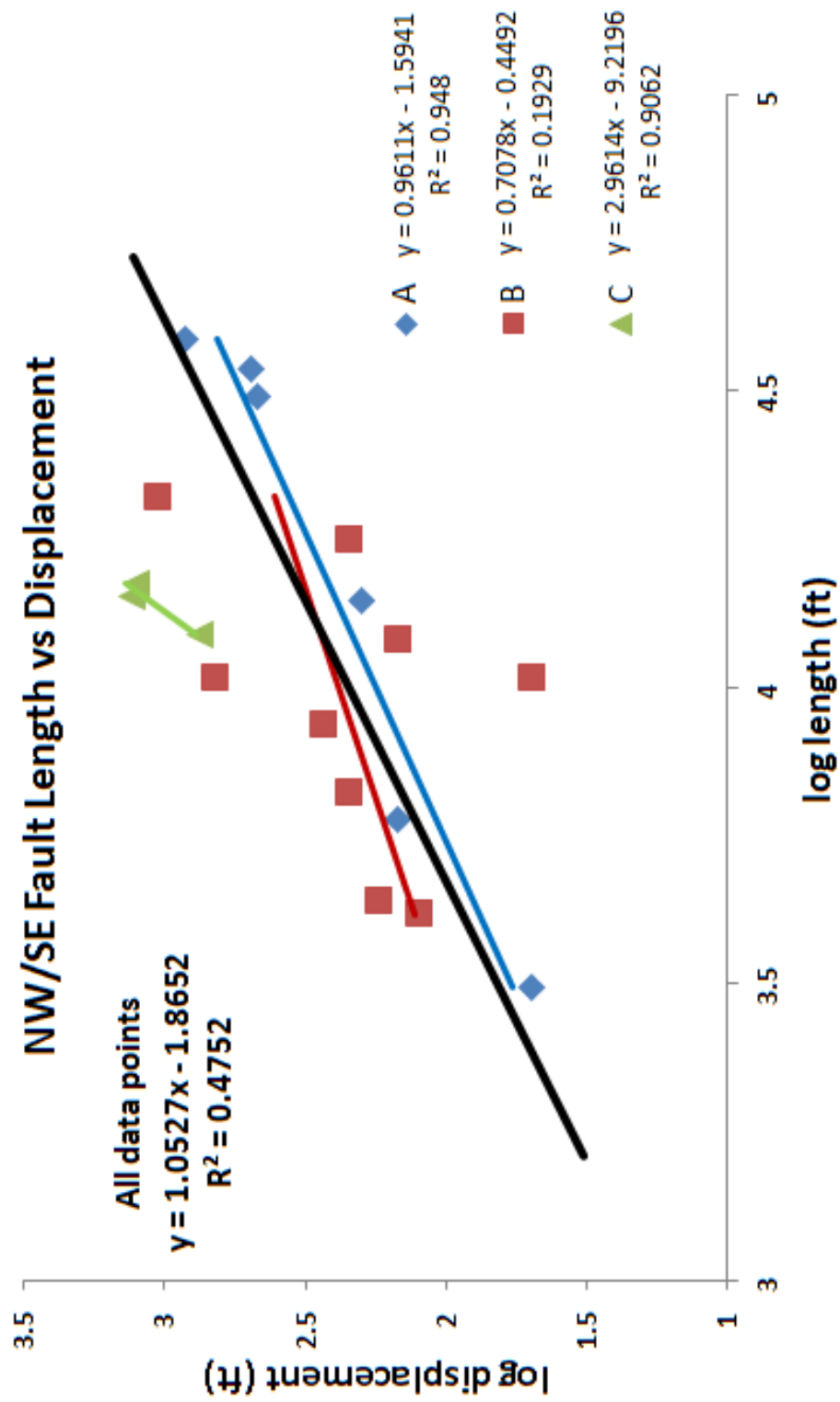


Figure 4.6: Log-log plot of fault length vs. displacement (dip-slip) for the deep NW/SE-trending faults; fault labels correspond to those in figure 4.1. Trendlines included for each fault set (color lines correspond to color of data symbols); black trendline represents all data points including points from faults 1, 2, 3, 4, & 6.

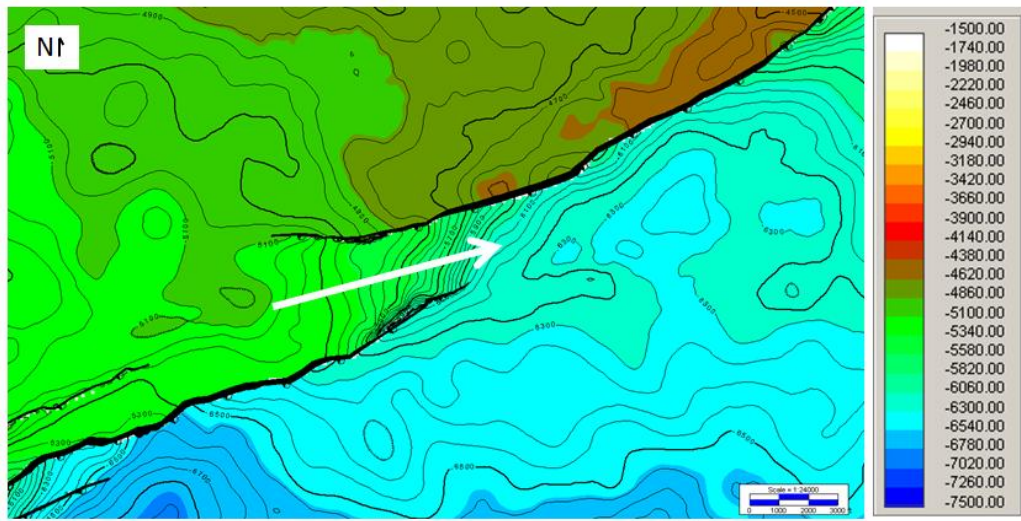


Figure 4.7: Depth structure map of the St. Peters (SSTVD, ft) illustrating typical steeply dipping relay ramp soft-linking two large faults; white arrows indicates dipping beds of the relay ramp before returning to regional dip.

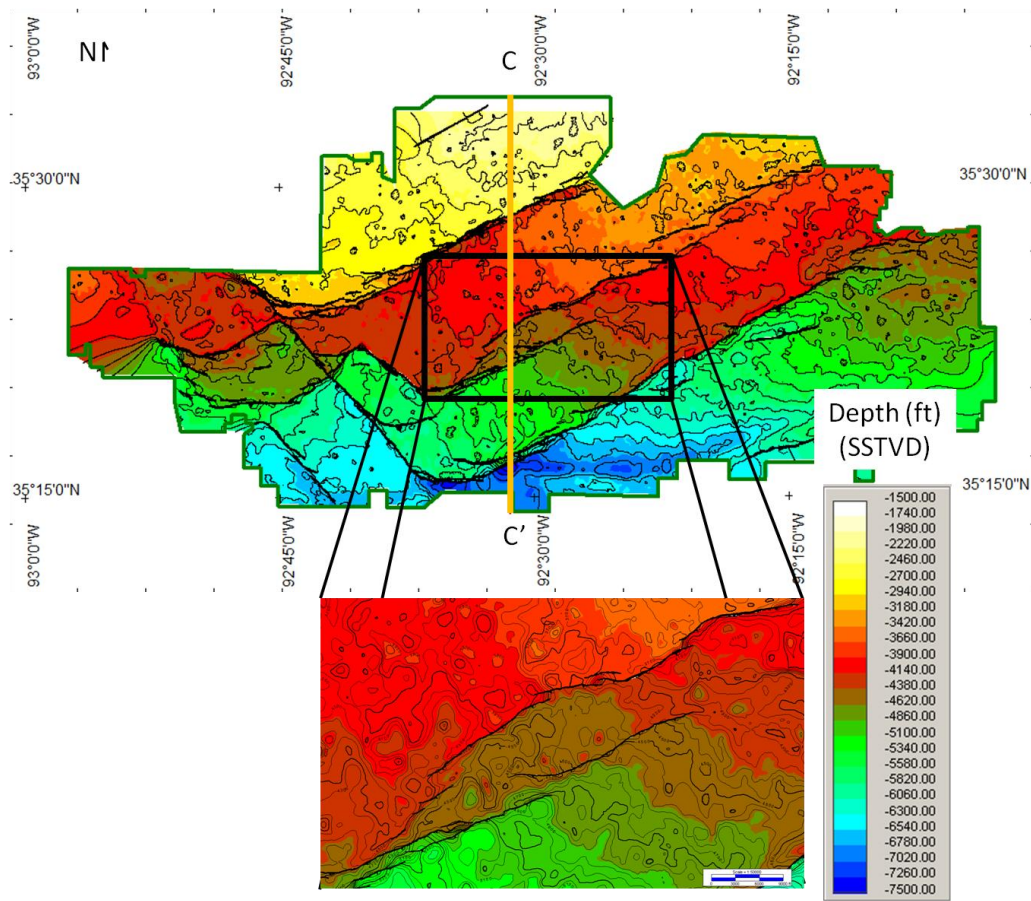


Figure 4.8: Depth structure map of the St. Peters illustrating anomalously large relay ramp along the central terrace fault (#3). Black lines – St. Peters fault polygons.

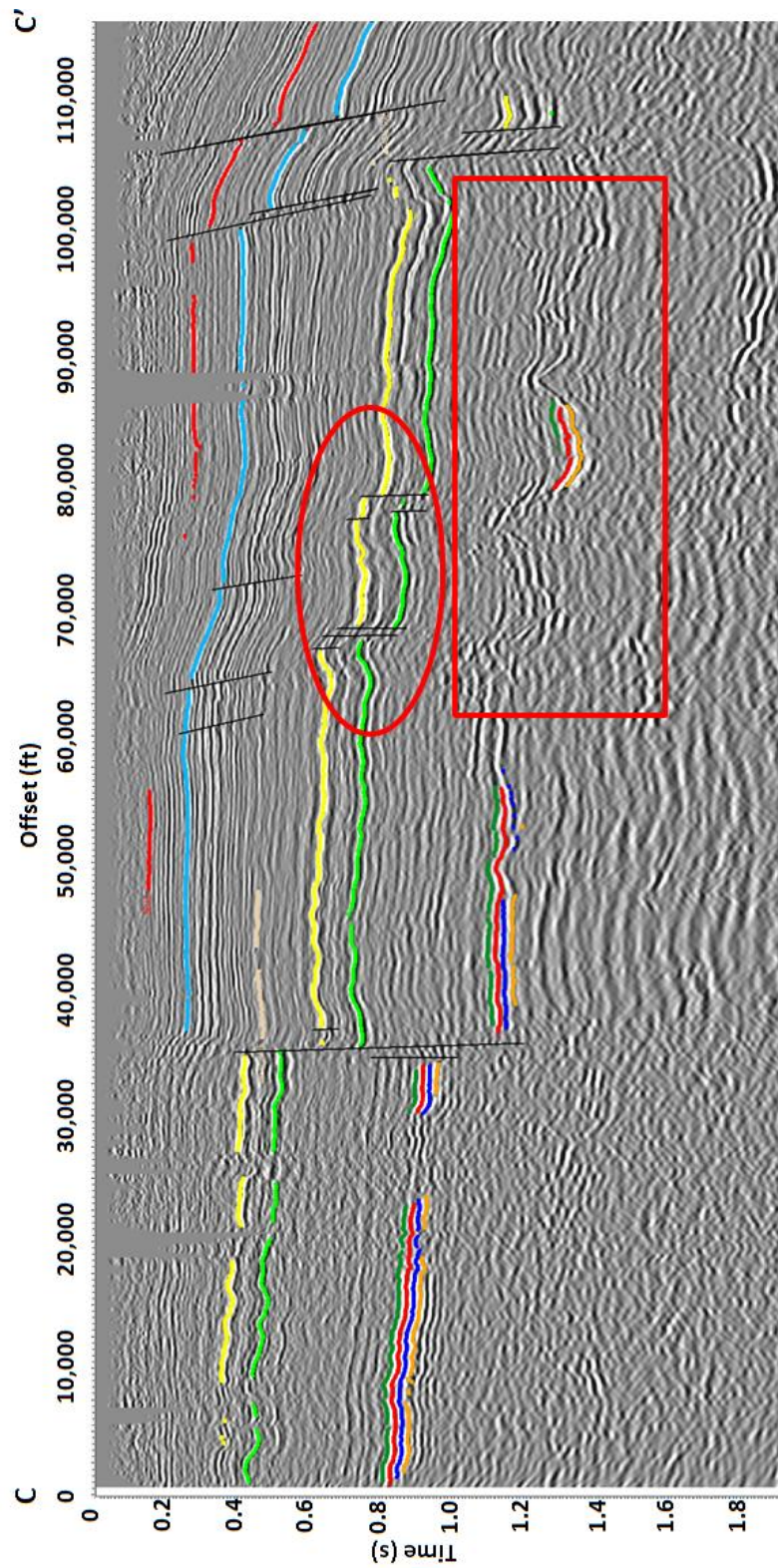


Figure 4.9: North/south line from WDM_AXIS_PSTM_Nat_filt_010611 volume indicating structural high below large relay ramp; black – deep and shallow faults; red – Sells, light blue – Orr; light brown – Basal Hale; yellow – Hindsville; light green – St. Peters; dark green, red, blue, and orange package of reflectors at depth – basement reflectors. Basement reflectors lose continuity within the red rectangle and are shallower in time than their surrounding corresponding reflectors. The red oval represents the large relay ramp structurally above the basement high.

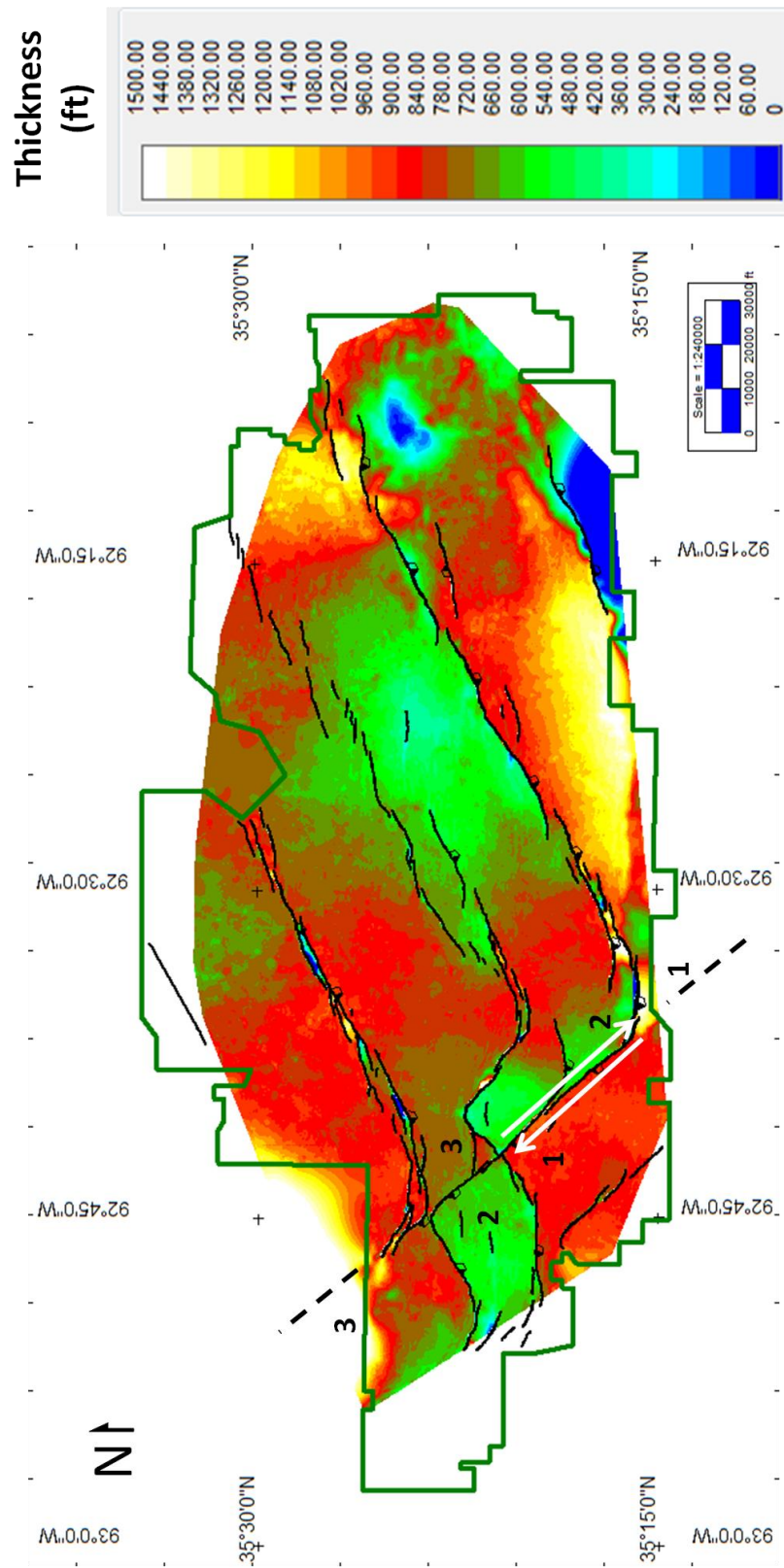


Figure 4.10: St. Peters to Hindsville isochore; numbers indicate corresponding fault blocks and white arrows indicate direction of block movement.

4.1.2 Shallow Structure

The Orr Sandstone depth structure maps in figure 4.11 illustrate the shallow structural regime. The shallow structure is characterized by primarily E/W-trending down-to-the-south normal faults with very little deviation in orientation and positioned in an en echelon array structurally above the deep fault traces. Structure generally deepens to the south and east. However, along the individual faulted terraces, the structure deepens southwest. The exact orientation distribution of the 129 interpreted faults in the shallow structure is illustrated in figure 4.12. The shallow faults tip out at depth into the Morrow and terminate up-section prior to the Sells or at the surface (figure 4.3). Thickening in the shallow section across faults is relatively minor with vertical expansion indexes close to one (figure 4.13 & 4.14). Only thickening towards the basin depocenter is observed. Shallow faults are less extensive in length and displacement compared with the deep faults (figure 4.15 & 4.16). The shallow faults also show increasing displacement as fault lengths increase. In general, shallow faults structurally over the NE/SW- trending deep faults have a larger maximum displacement than the shallow faults structurally over the NW/SE-trending deep faults.

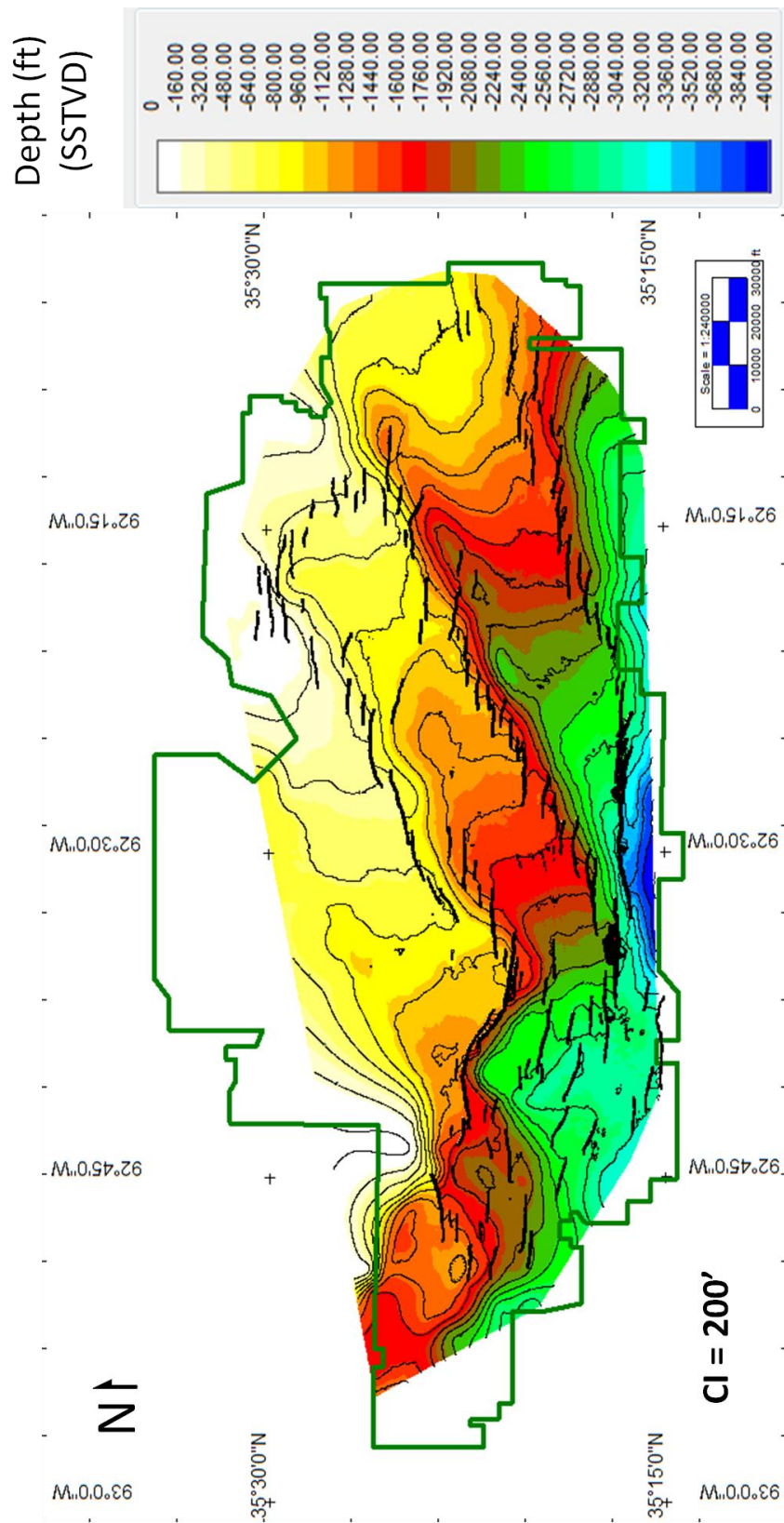


Figure 4.11: Orr depth structure map; thick black lines indicate interpreted faults.

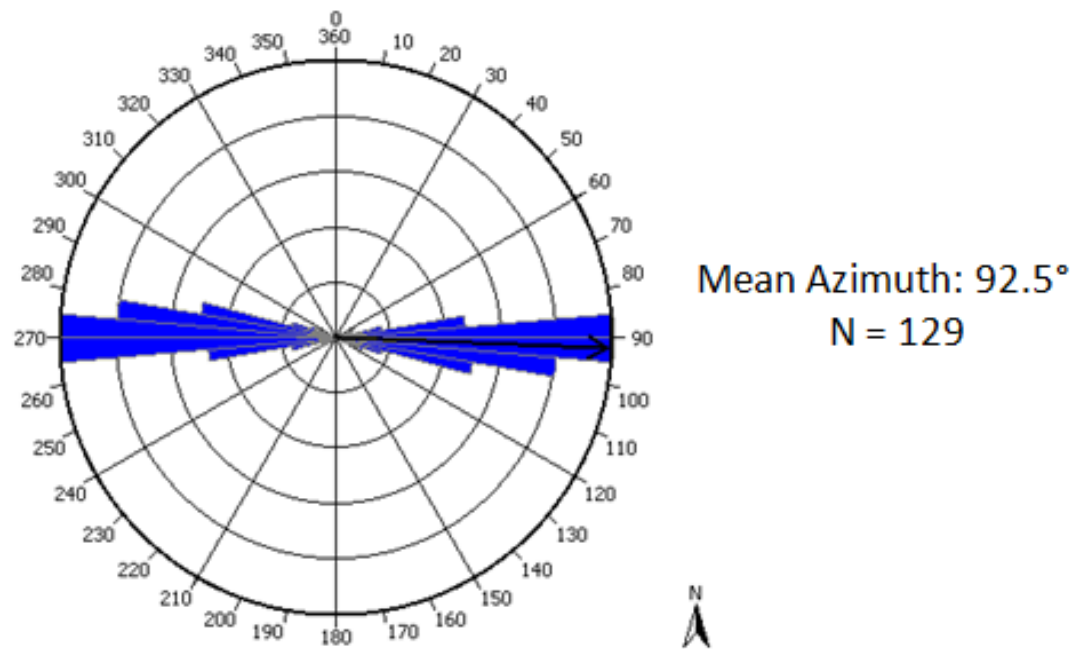


Figure 4.12: Shallow fault azimuth rose diagram (bidirectional); 129 faults interpreted to be penetrating the Orr Sandstone with an average orientation of 92.5° (black arrow). Unlike deep faults, the shallow faults are unimodal in an E/W direction.

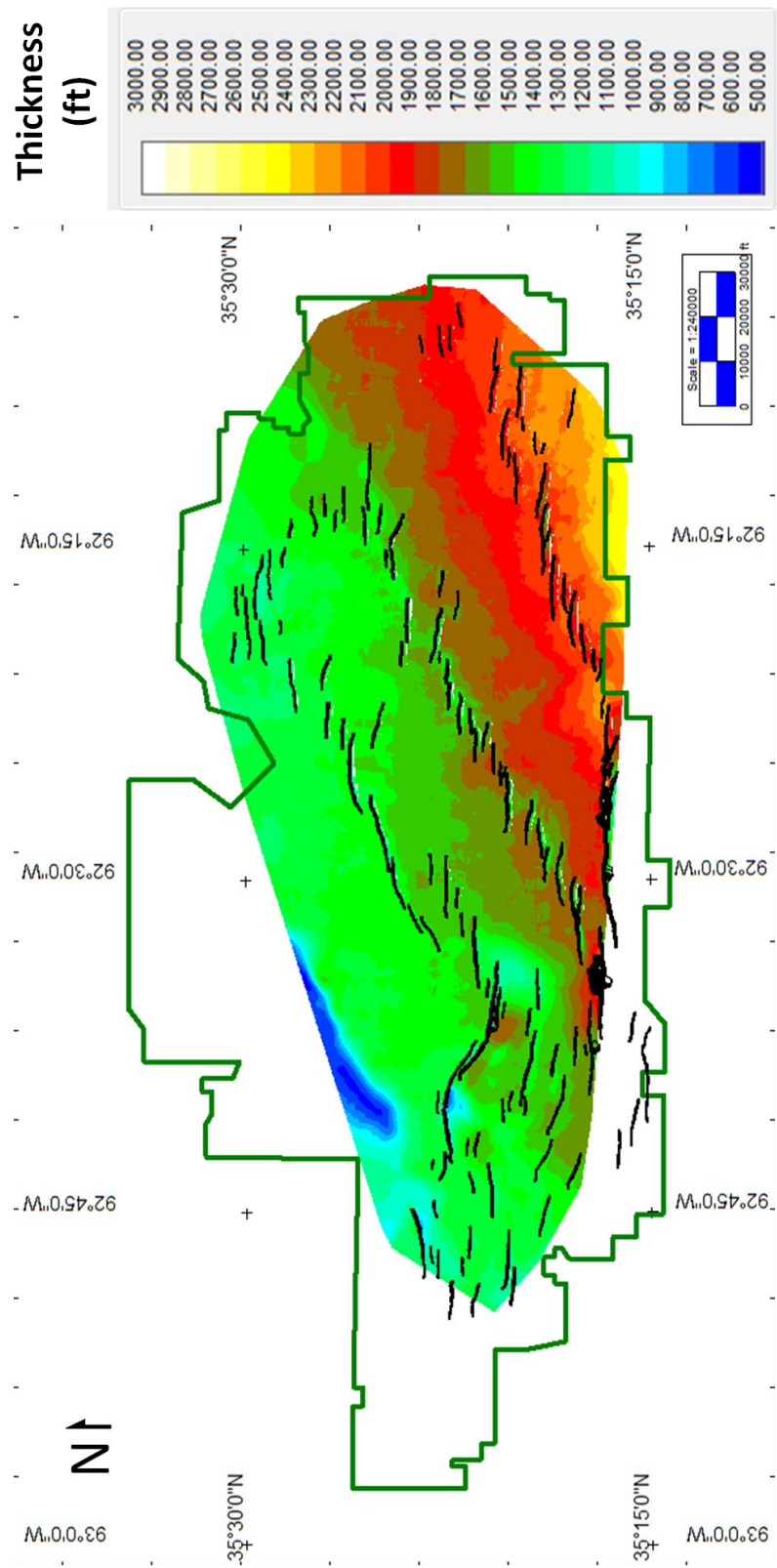


Figure 4.13: Basal Hale - Orr isochore; no appreciable thickening of section across faults. General thickening of the section does occur to the southeast towards the basin depocenter.

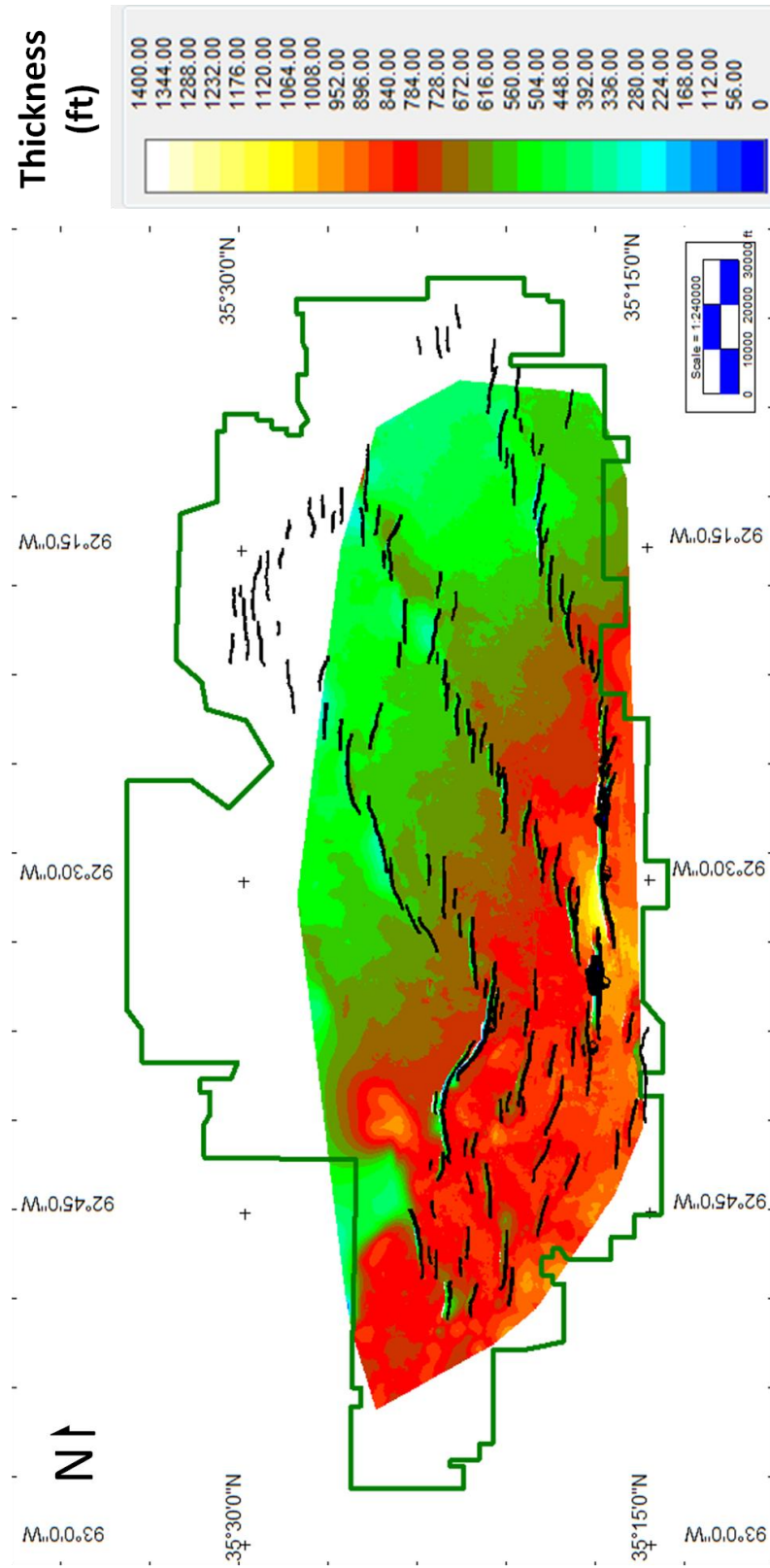


Figure 4.14: Orr- Sells isochore; no appreciable thickening of section across faults. General thickening of the section does occur to the southwest towards the basin depocenter.

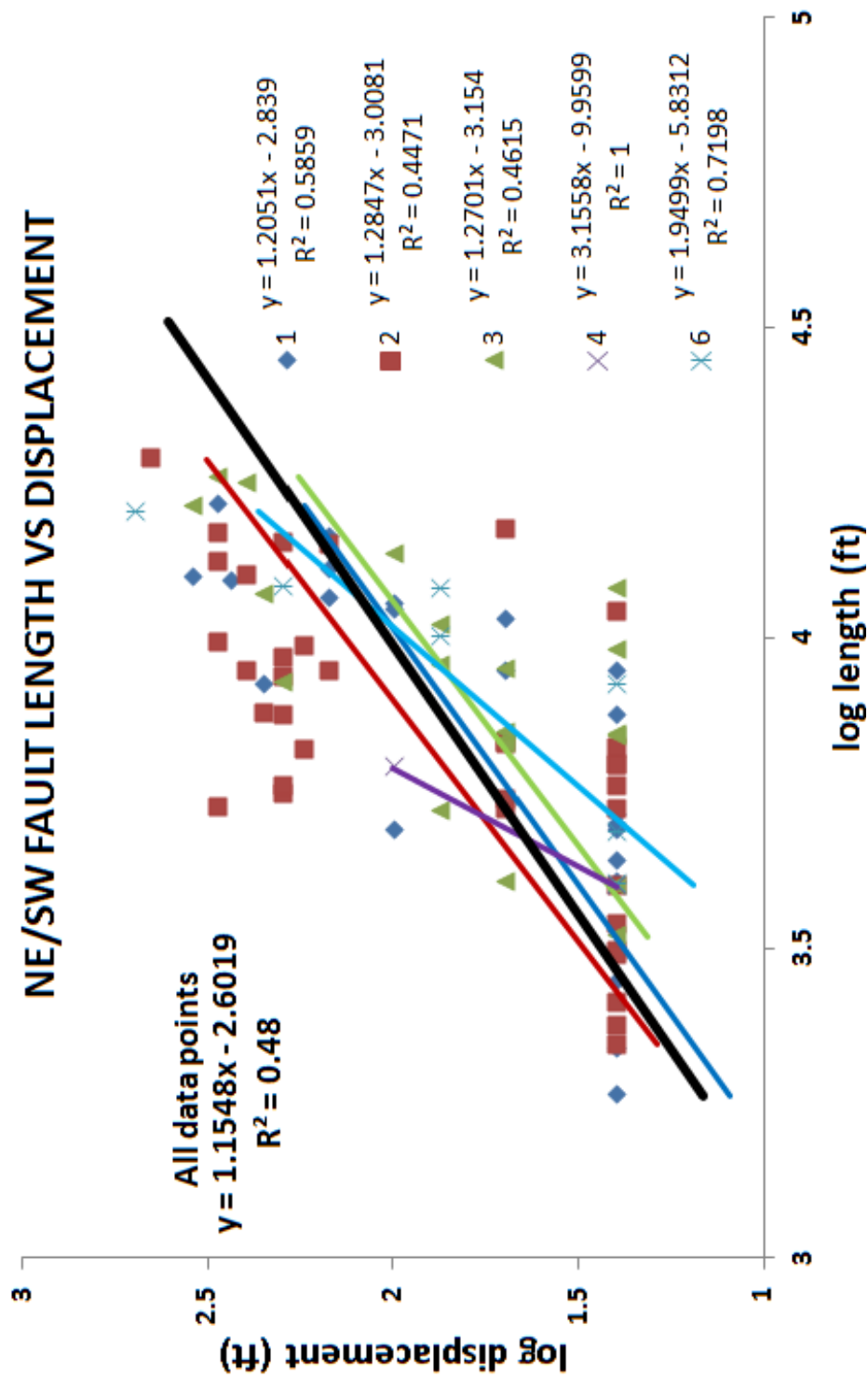


Figure 4.15: Log-log plot of fault length vs. displacement (dip-slip) for the shallow faults structurally above the NE/SW-trending deep faults; fault labels correspond to those in figure 4.1. Trendlines included for each fault set (color lines correspond to color of data symbols); black trendline represents all data points including points from faults structurally above faults A, B, & C.

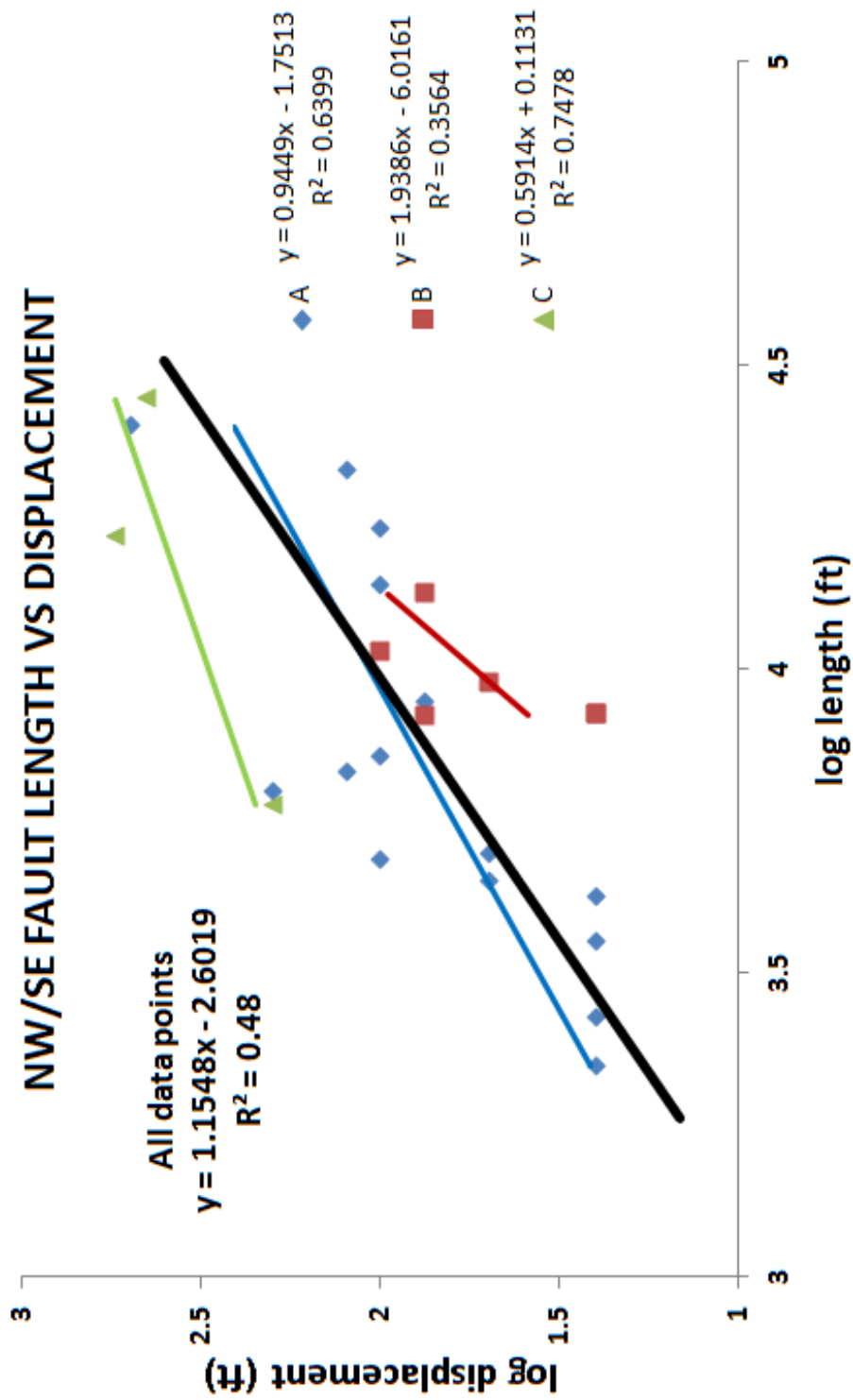


Figure 4.16: Log-log plot of fault length vs. displacement (dip-slip) for the shallow faults structurally above the NE/SW-trending deep faults; fault labels correspond to those in figure 4.1. Trendlines included for each fault set (color lines correspond to color of data symbols); black trendline represents all data points including points from the shallow faults structurally above faults 1, 2, 3, 4, & 6.

4.1.3 Fault Length and Displacement Implications

The log-log plots in figures 4.5, 4.6, 4.15, and 4.16 are set up similar to those developed by Clark and Cox (1996) to determine a systematic relationship between fault length and displacement. For this study, the log length and log displacement can be shown to have a linear relationship; however, the R^2 values for the trendlines are highly variable and not the best fit. The deep fault regime has a power law exponent in linear space (slope in log-log space) and a R^2 value of 1.05 and 0.48 respectively. The shallow fault regime has a power law exponent in linear space and a R^2 value of 1.55 and 0.48 respectively. For all faults in the area the power law exponent in linear space and R^2 value is 1.21 and 0.48 respectively (figure 4.17). There are three possible explanations for why the data has variable R^2 values. First, the number of samples is highly variable among fault terraces. Second, error may have been introduced by low resolution on seismic in determining exact position of fault tips and position of maximum displacement, potentially leading to over- and underestimates of fault lengths and displacements (Kim and Sanderson, 2005). Third, other authors use data sets from multiple sources that typically have data points scattered over 4 to 8 orders of magnitude in length and displacement (Cowie and Scholz, 1992; Marrett and Allmedinger, 1991; Watterson 1986). In contrast, the data set for this study only spans a little over 2 orders of magnitude.

In general, large fault systems are thought to be the result of linkage of smaller fault populations (Peacock and Sanderson, 1991; Dawers and Anders, 1995). For the deep structural regime in this study, the large fault lengths and displacements can be seen as small individual faults that have coalesced over time. Another reason for the low R^2 values for the large faults is that the individual faults may be in different states of strain and coalescence.

Unlike the deep faults, there are some shallow faults that have large aerial extents but very small displacements. One possibility for explaining this relationship is reactivation. Reactivation is renewed displacement after a period of inactivity produced by at least two distinct tectonic events (Peacock, 2002). Reactivation is a way that fault displacement geometries are modified and overlying previously deformed cover can have a controlling geometry and displacement from basement structures (Peacock, 2002). Peacock (2002, figure 12a) illustrates what will occur to the log-log plots for length and displacement of fault populations that are reactivated from a previous extensional environment. In the case of normal dip-slip reactivated to strike-slip, faults should cluster towards a larger length measurement while dip-slip only increases or decreases slightly. Conversely, it can be implied that strike-slip faults reactivated to normal dip-slip will have the inverse relationship, similar to the shallow faults seen in figures 4.15 and 4.17.

ALL FAULTS

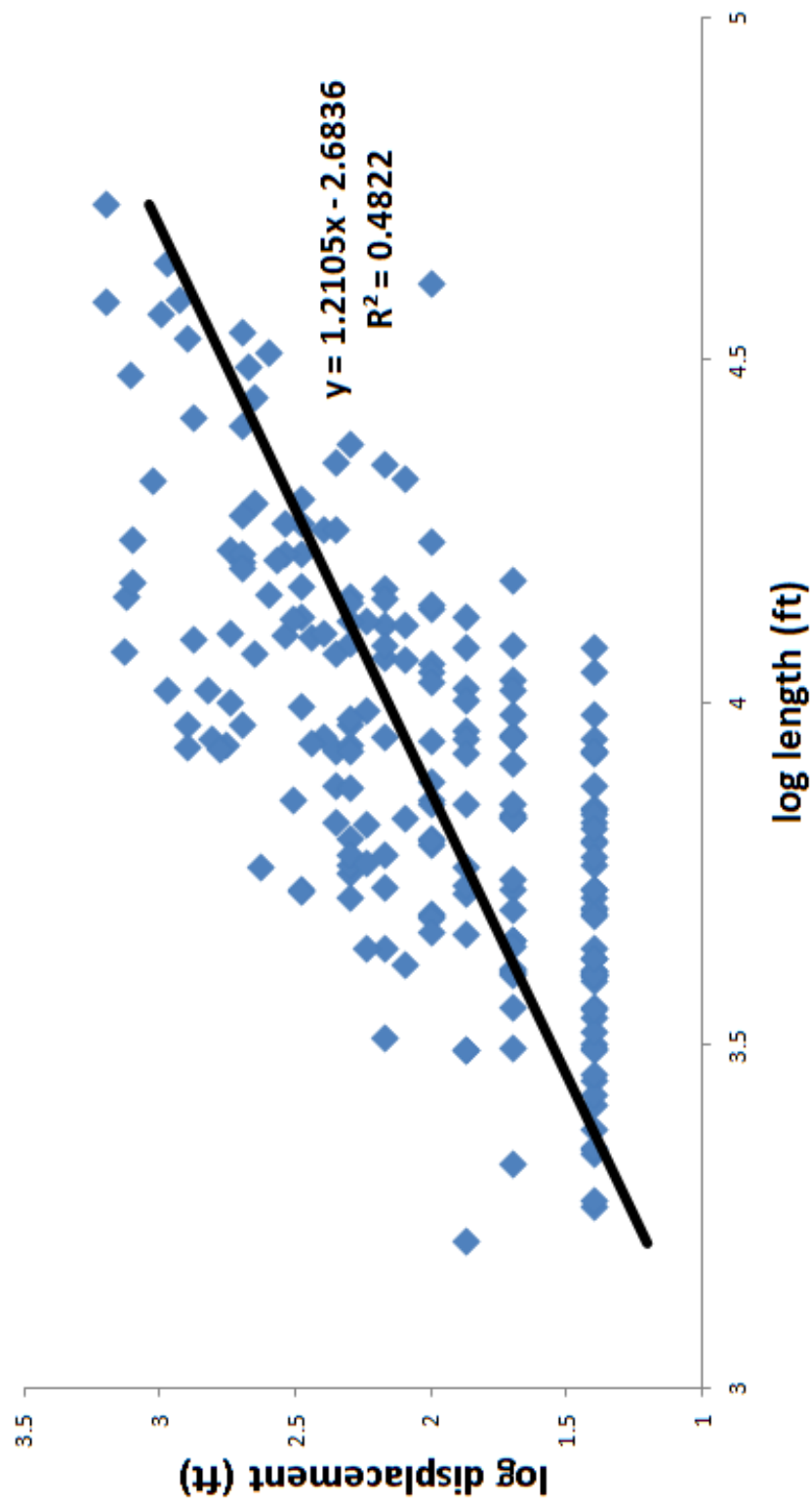


Figure 4.17: Log-log plot of fault length vs. displacement (dip-slip) for all faults within the study area. Black trendline represents all data points.

4.2 Linking the Deep and Shallow Structure

In cross-sectional view deep faults lie structurally below shallow faults with only minor lateral offset (figure 4.3). The close proximity of the separate fault regimes indicates that the deep faults did control formation of the shallow faults, but not from a pure dip-slip motion along the deep faults. In map view, the shallow faults are positioned in an en echelon array structurally above the deep faults (figure 4.18). A closer look at the orientation and spatial variation of the shallow faults is comparable to both models used to describe generation of Riedel shears and tension gash fractures (figure 4.19). When maximum horizontal stress (σ_1) is oriented in an E/W orientation, fractures should open in the N/S direction of minimum horizontal stress (σ_3). In the same manner, the Riedel shearing model indicates that if there is an imposed shear from an underlying plane of weakness, fractures will preferentially generate in an orientation of 15°, -10°, & 75° away from the imposed shear plane. The two antithetic, deep faults in figure 4.19 line up almost identically to the 15° R shears; however, the shallow faults shear at an angle closer to 28°. Because there is a transition from a more competent carbonate section at depth to a less competent clastic section near the surface, the fractures generated in the shallow clastic section should not mimic the Riedel shear model exactly. However, a primarily E/W oriented regional compression would generate strike-slip along the deep faults inducing a more local stress oriented parallel to the deep fault traces. This local maximum principal stress oriented along the deep fault traces would invoke the Coulomb fracture criterion that rocks under confining pressure develop shear fractures in an approximate orientation of 30°.

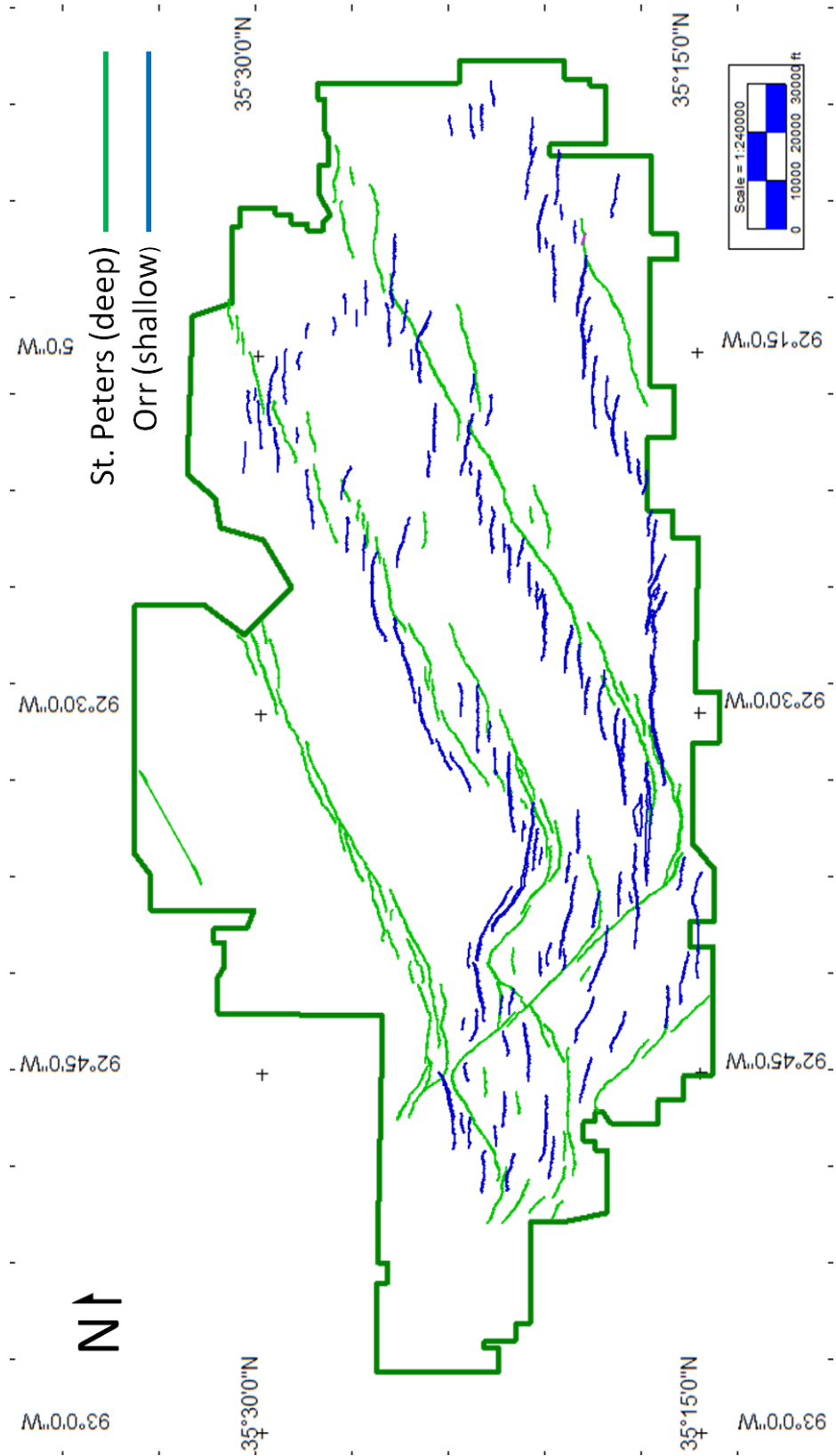


Figure 4.18: Co-rendered St. Peters and Orr polygon fault maps.

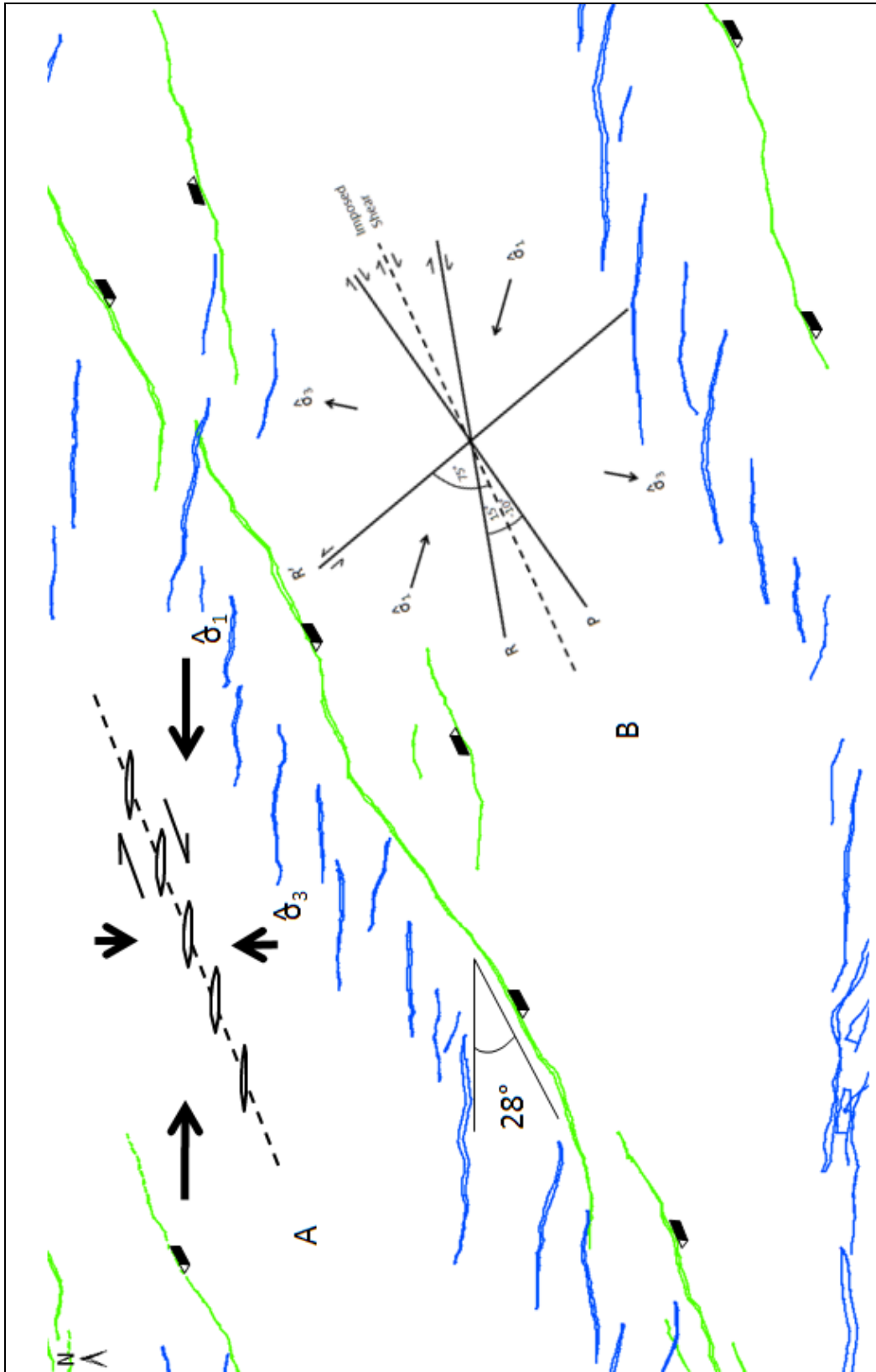


Figure 4.19: Green lines – St. Peters fault, blue lines – Orr faults; (A) Gash fracture generation model (modified from Twiss and Moores, 2007) and (B) Riedel shear generation model modified from Freund 1974; Orr faults generate at an angle of 28° to the imposed shear plane.

Because the shallow faults predominately have a different orientation than the deep faults, it is assumed that the deep faults did not control the formation of the shallow faults with dip-slip motion; however, there are some exceptions to this rule. Shallow faults along the northern extent of the large relay ramp associated with fault terrace 3 and shallow faults along fault C have identical orientations as the underlying deep faults (figure 4.20). In this case, dip-slip is the primary component of displacement along the shallow faults.

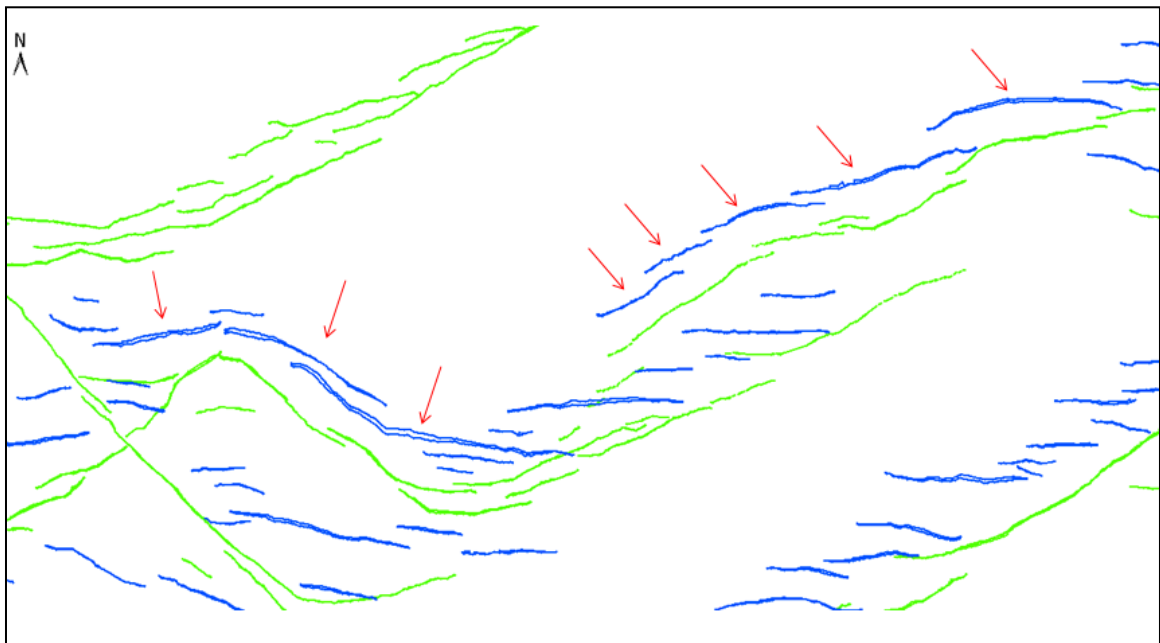


Figure 4.20: Green lines – St. Peters fault, blue lines – Orr faults, red arrows – shallow faults with same orientation as underlying deep faults.

While the deep structure did not control shallow faulting during deposition, indicated by lack of growth faulting, the deep faults do in fact control the shallow structure. Figure 4.21 illustrates the largest amount of relief in the shallow structure to be positioned directly above the deep fault traces. Shallow structure also deepens to the southwest along the individual fault blocks with the largest amount of relief occurring to the southwest also. To the northeast, the relief in the shallow structure becomes less.

4.3 Relative Timing

Developing a model for fault generation and relative timing for the study area is difficult because faults typically die out into strata that have low resolution or at the near surface on seismic. Fault timing is also difficult to determine because strata younger than early Pennsylvanian were never deposited or have been removed. However, there are multiple indicators observed in the general structure section that suggest relative timing for both sets of faulting.

Figure 4.3 shows a colluvial wedge formed in the hanging wall block of the Morrowan Shale. Figure 4.22 shows the colluvial wedge in a zoomed-in cross-sectional view. The thinning and thickening seen in the Morrow extends the entire trace of the faults and is fairly uniform in thickness (figure 4.4). Movement seen along the deep faults must have occurred around the Mississippian-Pennsylvanian boundary because the Morrow is thinned in the footwall block and thickened in the hanging wall block from subaerial or submarine erosion.

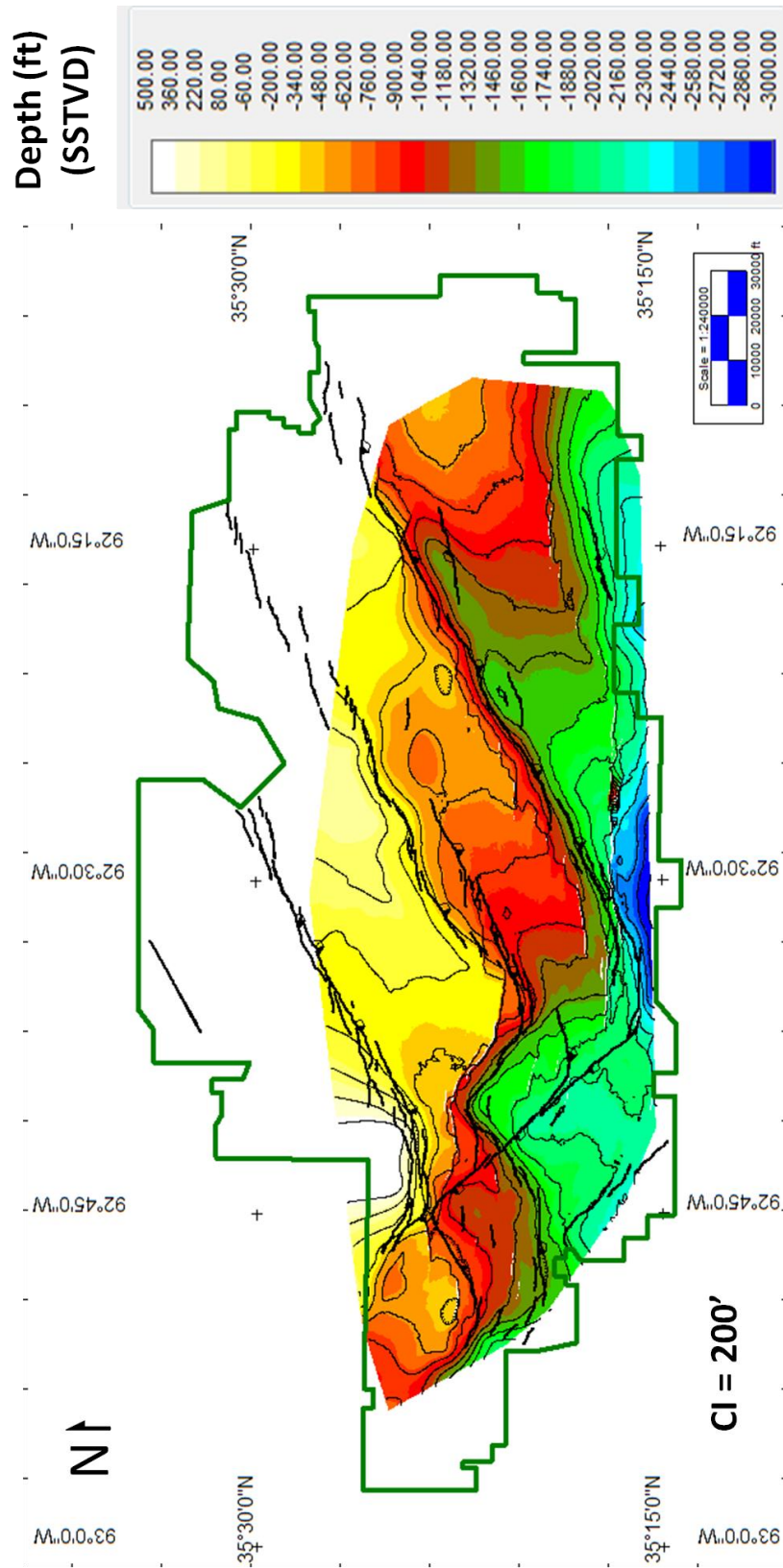


Figure 4.21: Sells depth structure map overlain with St. Peters fault polygon.

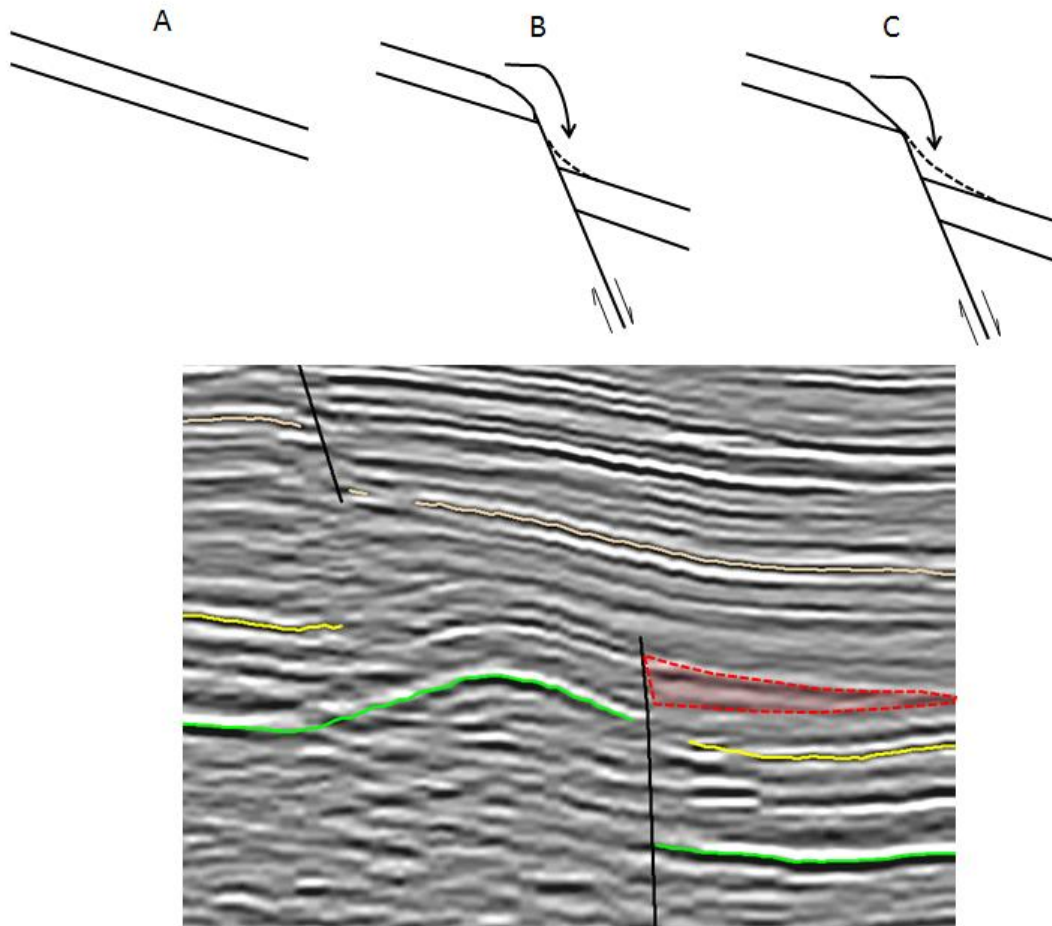


Figure 4.22: (Top) Colluvial wedge formation: solid arrow denotes removal of footwall block to form the wedge. (A) undeformed bedding prior to fault generation; (B) intermediate stage where displacement has occurred along normal fault creating a zone of accommodation for material eroded from the footwall block; (C) continuation of stage B until movement along the fault has ceased or hill slope created by the eroded footwall block and formed colluvial wedge reaches equilibrium (modified from Morey and Schuster 1999). (Bottom) Example of Morrowan Shale colluvial wedge on seismic; red outline- colluvial wedge, green – St. Peters Limestone, yellow – Hindsville Limestone, and tan – Basal Hale Sandstone.

The strike-slip displacement along fault A occurred near the end of the Mississippian-Pennsylvanian boundary. Fault A is hypothesized to have moved at this time because there are no overlying structures in the shallow section and only minor dip-slip has occurred across the deep structure (figure 4.1). Movement was dominated by strike-slip displacement. In general, if there is a common variation in unit thickness across a fault, offset may be illustrated as a discontinuity on an isochore map (Twiss and Moores, 2007; figure 4.23). According to the isochore in figure 4.10, potentially 9 miles (14.5 km) of strike-slip displacement may have occurred along fault A. Strike slip movement also must have occurred before deposition of the Basal Hale Sandstone. If the shallow structure was deposited prior to strike-slip movement, strike-slip duplex structures or rotated fault traces should be present in the shallow structure. Neither flower structures nor fault rotation is seen in the lower Pennsylvanian section (figure 4.11).

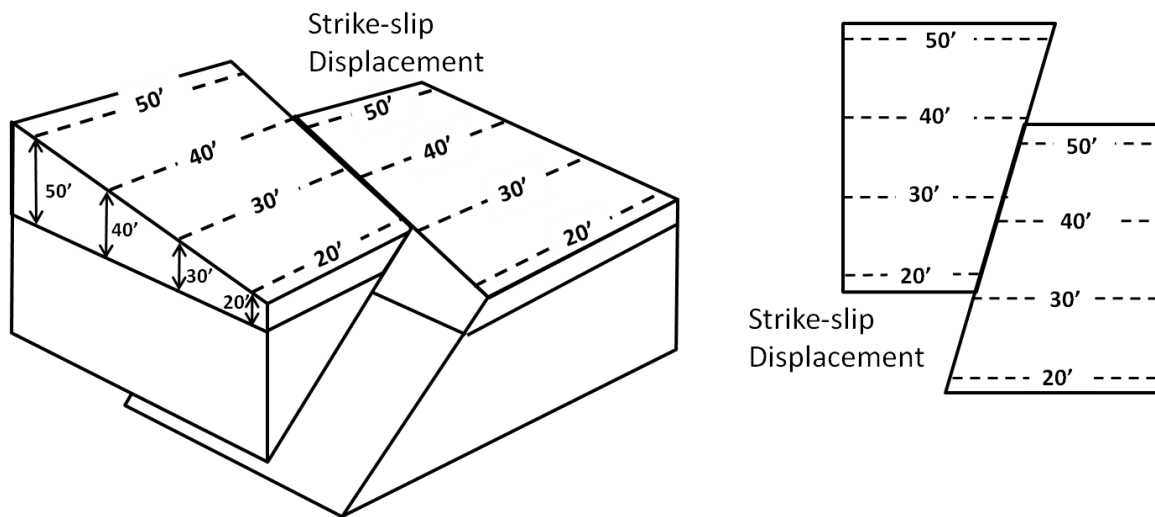


Figure 4.22: (Left) Theoretical block diagram illustrating amount of slip using an isochore map; (Right) Map view of the block diagram showing thickness contours for determining slip (modified from Twiss and Moores, 2007)

Following deposition of the shallow, Early Pennsylvanian section, reactivation of the deep NE/SW-trending faults in a dextral-slip motion generated fractures in the overlying shallow structure. Transition of the predominately N/S compression associated with the Ouachita orogeny in the Middle Pennsylvanian to the E/W compression associated with the Alleghenian orogeny up to the Late Permian generated the en echelon array of fractures in the shallow section. Because the regional stress field was E/W oriented compression, it is unlikely that extension occurred in a N/S direction in the shallow structure at this time. A later extensional stress regime was responsible for generating normal dip-slip on the shallow formed fractures.

The final period of extension occurred in the Mesozoic. Rifting of the southern margin just north of the Louisiana-Arkansas border reactivated the deep faults and generated dip-slip displacement along both the deep and shallow faults. This late stage movement is hypothesized because of the cross-cutting relationship fault 6 has with fault A (figure 4.1), and the select few shallow faults that follow the exact same orientation as their underlying counterpart (figure 4.20).

4.4 Structural Model

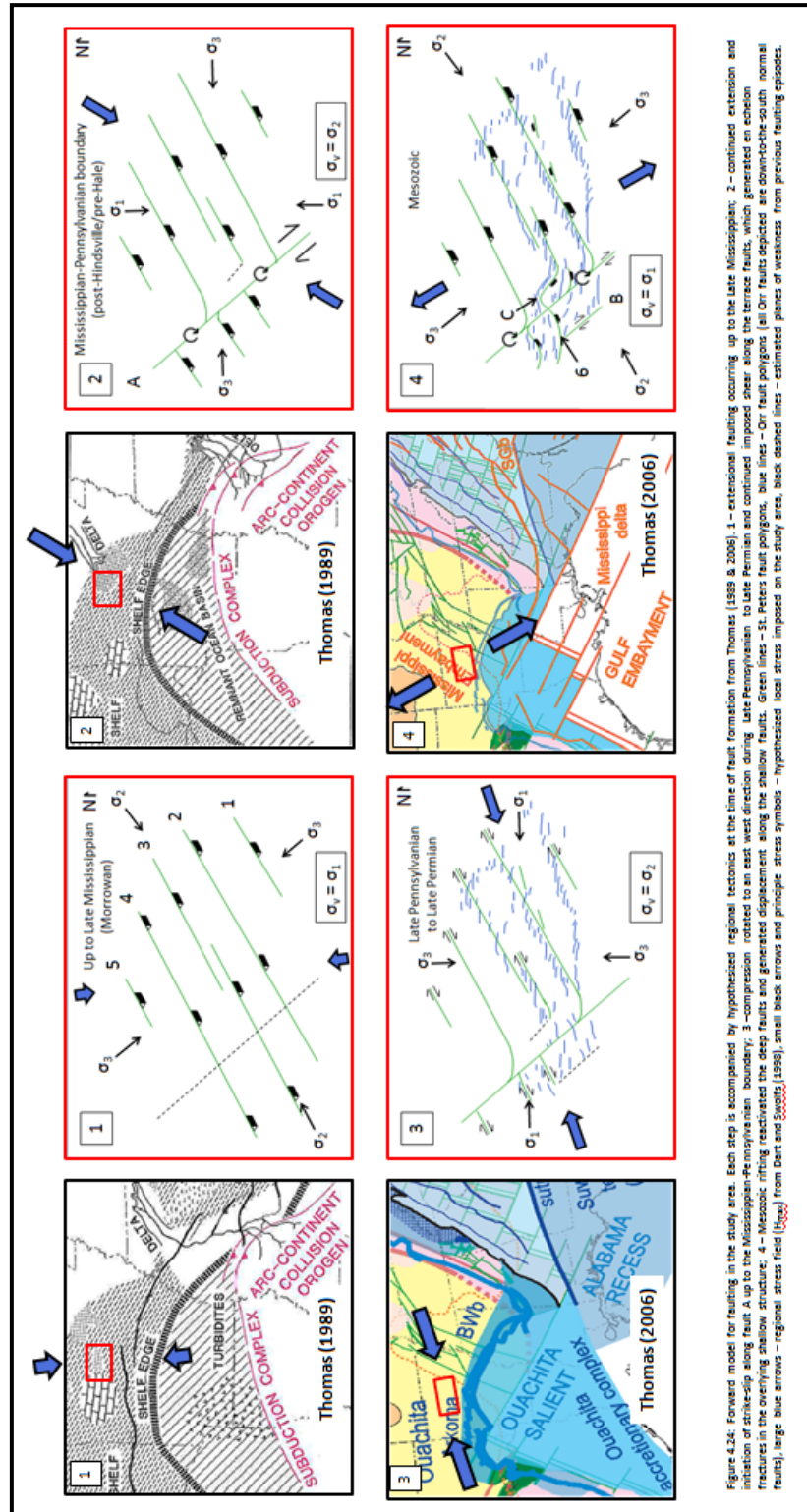
The structural model presented here describes the deformation observed in the study area to have occurred between the Late Mississippian to the Mesozoic (Figure 4.24); the deformation of the study area is as follows:

1. Early stages of rifting during the late Proterozoic to early Cambrian potentially left behind NE/SW-and NW/SE-trending planes of weakness that preferentially determined position of the deep set of faults interpreted. Timing of onset for flexural downwarping along the continental margin is difficult to identify. Crustal loading generated a

maximum vertical stress north of the fold and thrust belt to form the large down-to-the-southeast normal terrace faults around the Late Mississippian.

2. A transition from predominantly N/S compression to a more NE/SW directed compression continued in the Late Mississippian to the Early Pennsylvanian. This transition occurred sometime following deposition of the Hindsville but before deposition of the Hale sands. This transitional period is being hypothesized to satisfy generating large strike-slip displacement along the central NW/SE-trending fault A. Figure 4.10 illustrates similar thicknesses for fault blocks bounding fault A and suggest amount of slip. The Orr depth structure map in figure 4.11 also suggests that major movement occurred prior to deposition of Pennsylvanian clastics, since there are no major overlying structures (i.e.: flower structures) or rotation of any shallow faults traversing fault A. Fault A's strike-slip displacement may have generated parallel planes of weakness for later faulting (i.e.: fault C). Locally along the trace of fault A, the fault blocks on either side probably experienced some clockwise motion.
3. Shallow clastics, at least up to the Sells, were deposited during the Early to Middle Pennsylvanian time frame (Lower Atokan). Throughout the Late Pennsylvanian and into the Late Permian, the regional stress field is hypothesized to have rotated to ENE/WSW direction. At this time, NW/SE extension subsides and E/W compression begins to dominate, primarily because there is no appreciable thickening seen in the Lower Atokan units. Continued compression initiated fractures in an en echelon array within the Lower Atokan units. The shift in stress field prolonged the development of fractures in both the deep and shallow structure.

4. Finally, Mesozoic rifting with primarily NNW/SSE extension created the normal displacement along the previously fractured en echelon faults. This extension also generated a few antithetic faults in the deep structure. Extension at this time is also responsible for the large normal fault that cross-cuts fault A and all of the shallow faults with the same orientation structurally above the deep faults. Continued extension may have allowed fault C southwest of fault A to generate. Continued strike slip displacement along this plane of weakness may explain why shallow faults in the southwest portion of the study area have western fault tips that are rotated clockwise to a more NW trend. Furthermore, figure 4.21 reinforces the hypothesis that there was a late stage extensional event that created large structural relief in the shallow section that directly correlates to the deep fault traces.



5 Discussion

5.1 Implications for the Tectonic Evolution of the Arkoma basin

Do the current structural models accurately describe the tectonic evolution of the Arkoma basin? This was the question posed prior to the inception of this research. Two significant papers dealing with the formation of the Arkoma Basin are Houseknecht (1986) and Van Arsdale and Schweig (1990). The fundamental difference between the structural model generated in this thesis and those described by Houseknecht and Van Arsdale and Schweig is post-Ouachita deformation. Deformation in the Arkoma Basin is thought to have terminated around the Late Pennsylvanian (Van Arsdale and Schweig, 1990) or Desmoinesian (Houseknecht, 1986). It is quite possible that the Arkoma Basin has not experienced significant deformation after cessation of the Ouachita orogeny; however, post-Ouachita deformation should at least be considered. Post-Ouachita deformation is being considered because of the interpreted 3D orientation of faults and lack of syntectonic deposition in the study area.

Van Arsdale and Schweig (1990) recognized that the deep set of faults in the eastern Arkoma Basin strike in a NE/SW direction before returning to a predominately E/W strike further east and west of the interpreted seismic lines. However, 3D seismic reveals that faults A, B, and C in figure 4.1 strike in a NW/SE direction before returning to an E/W strike further west. Also, in cross-sectional view, there is no way to observe that the shallow listric faults are not the same orientation as the deep faults. In fact, there must have been some strike-slip movement along the deep faults to generate the en echelon array of shallow faults structurally above the deep faults. It follows that syntectonic deposition may or may not have occurred in the eastern portion of the basin. It is known from well logs that the deep faults in the western portion of the basin were active during rapid sedimentation (Houseknecht 1986). However, the lack of strata at

the surface prohibits research on whether or not faults were active during deposition of the Middle-Late Atokan sediments for the eastern portion of the basin. So going back to Van Arsdale and Schweig's original conclusion, the geometry of the eastern Arkoma Basin is in fact different from the western portion of the basin.

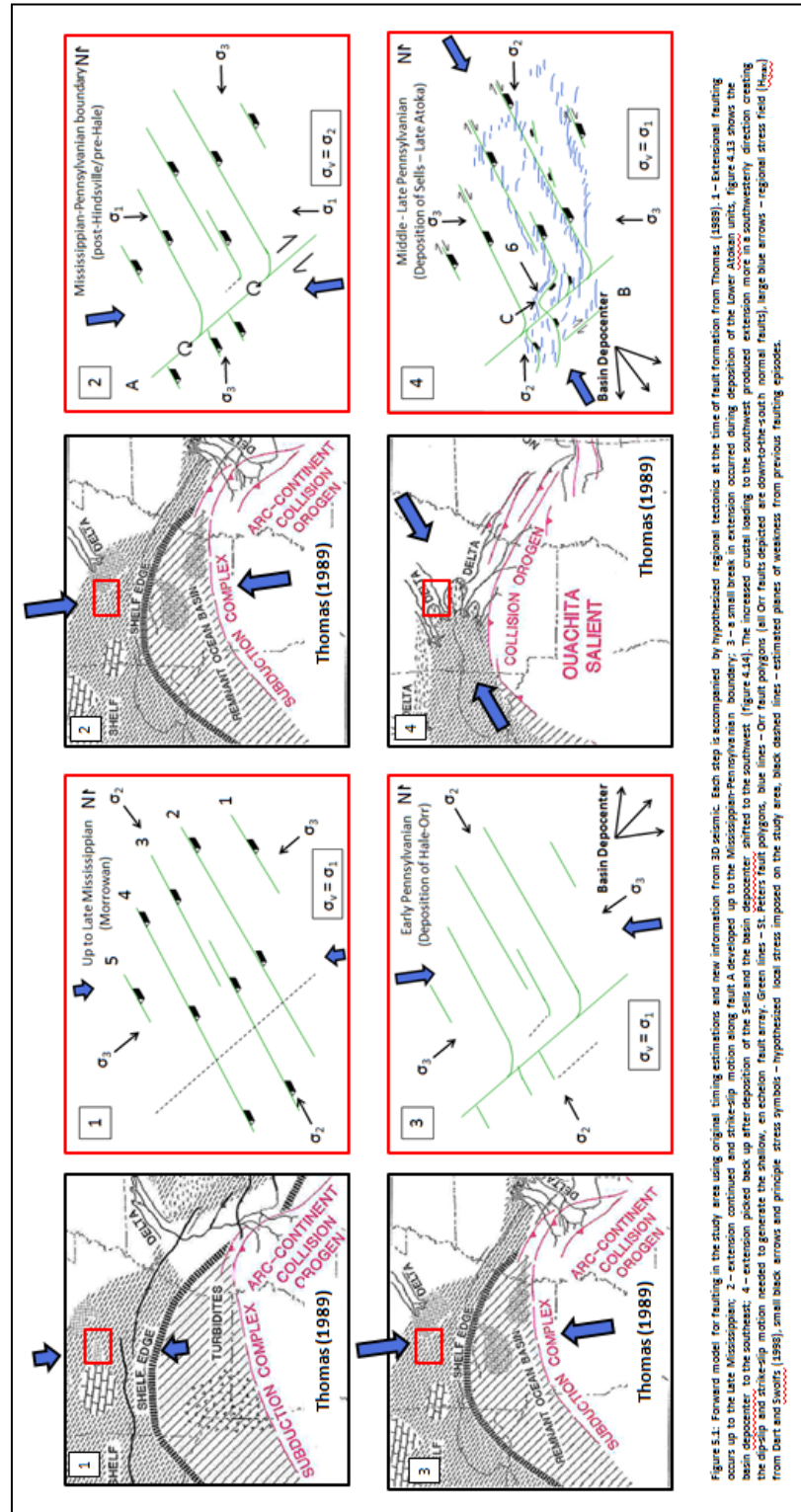
The next important factor in determining accuracy of the structural model is timing. A new structural model inferring timing of fault generation and movement for the eastern basin was developed as shown in figure 4.24. Using the new information from the 3D interpretation, can a structural model be built that is kinematically correct and satisfies deformation only up to Desmoinesian time?

The hypothesized structural model confines deformation seen in the study area from Late Mississippian to the Desmoinesian (Figure 5.1); the deformation of the study area is as follows:

1. Early stages of rifting during the Late Proterozoic to Early Cambrian potentially left behind NE/SW- and NW/SE- trending planes of weakness that preferentially determined position of the deep set of faults interpreted. Timing of onset for flexural downwarping along the continental margin is difficult to identify. Crustal loading generated a maximum vertical stress north of the fold and thrust belt to form the large down-to-the-southeast normal terrace faults around the Late Mississippian.
2. N/S compression and crustal loading continued into the Late Mississippian to the Early Pennsylvanian. This continued compression generated large strike-slip displacement along the central NW/SE-trending fault A. Figure 4.10 illustrates similar thicknesses for fault blocks bounding fault A and imply amount of slip. The Orr depth structure map in figure 4.11 also implies that major displacement occurred prior to deposition of Pennsylvanian clastics, since there are no major overlying structures (i.e.: flower

structures) or rotation of any shallow faults traversing fault A. Fault A's strike-slip movement may have generated parallel planes of weakness for later faulting (i.e.: fault C).

3. Shallow clastics were deposited during the Middle Pennsylvanian (Lower Atokan). In contrast to figure 4.24, rotation of the regional stress field has not occurred yet. A short hiatus in faulting is experienced in order to deposit the Hale to Orr section without any significant thickening across the shallow faults. During this time the basin depocenter is located to the southeast of the study area (figure 4.13).
4. Finally, the regional compressive stress field is hypothesized to have rotated clockwise to a more NE/SW direction along with a shift in the basin depocenter to the southwest (figure 4.14). Oblique-slip displacement is generated along the NE/SW trending terrace faults that generated the shallow set of faults in an en echelon pattern. This extension also generates a few antithetic faults in the deep structure. Extension at this time is also responsible for the large normal fault 6 that cross-cuts fault A and all of the shallow faults with the same orientation as their underlying deep counterparts. Continued extension may have allowed fault C southwest of fault A to generate. Clockwise rotation near fault A from strike-slip displacement may explain why shallow faults in the southwest portion of the study area have western fault tips that are rotated clockwise to a more NW trend. Furthermore, figure 4.21 indicates a final extensional event that created large structural relief in the shallow section that directly correlates to the deep fault traces.



The major difference between the two proposed structural models is timing and orientation of the regional stress field driving deformation. In both models, the regional stress field showing maximum horizontal stress was determined from interpreted deformation within the Reelfoot Rift (Dart and Swolfs, 1998). With the added 3D seismic interpretation, determining the sequence of faulting is not too difficult. In both models the sequence of faulting and displacement does not change; however, the applied stress field and the manner and timing in which faulting occurs does change. The stress fields hypothesized in figures 4.24 and 5.1 differ from Dart and Swolfs (1998) because transitional fields are needed to explain kinematics and deformation of the eastern basin. Also, all extension seen in the second model (figure 5.1) is caused by crustal loading from the obducting Ouachitas. In the first model (figure 4.24), extension is generated by crustal loading in initial stages and rifting to the south in the final stage. Also, with the second model not progressing in time past the Desmoinesian, rotation of the stress field is potentially nominal.

5.2 Reactivation, Crustal Loading, and Crustal Flexure

The possibility that pre-existing planes of weakness from earlier periods of deformation have experienced additional movement through fault reactivation from different stress regimes was essential in developing the two structural models. Making this assumption implies that the stress field in the study area has previously caused the rock to exceed its original shear stress (τ_1) and only has to exceed a new shear stress (τ_2) that is lower than the original to produce subsequent movement along the same fault or plane of weakness. In this case τ_1 is designated as the Coulomb fracture criterion when $\tau_1 = \tau_0 + \sigma * \tan\phi$, where τ_0 is the cohesive strength of the rock, σ is the normal stress, and $\tan\phi$ is coefficient of internal friction. For reactivation, τ_2 can either be $\tau_2 = \tau_0^* + \sigma * \tan\phi^*$ where τ_0^* and $\tan\phi^*$ are the new cohesive strength and

coefficient of internal friction if the fracture/fault has been cemented, or $\tau_2 = \sigma * \mu$ where μ is the coefficient of sliding friction. In the study area, it is being assumed that τ_1 has been exceeded for the oblique-slip displacement along the large terrace faults, the major strike-slip movement along the NW/SE fault A, and the vertical displacement along the shallow faults, and that subsequent movement is falling under some hypothesized τ_2 .

It is important to note that the idea of zone of weakness or pre-existing plane of weakness has been somewhat misused in past literature. Stearns et al. (1981) states:

“A casual reading of geological literature indicates a widespread misuse of the concept of zone of weakness (that is, the reactivation of old faults in a new deformation period). Many geologists believe that once a fault exists in a rock mass, any new deformation phase, no matter what the orientation of the stress field, will surely cause reactivation.” (p. 218)

However, for this study, assuming reactivation of pre-existing planes of weakness is highly probable. Actual calculation of the ancient stress fields would be difficult to determine for the study area, but generalized direction of stress and previously formed structures can be used to make a strong case for reactivation instead of relying quantitatively on the fracture criterion.

Planes of weakness for the NW/SE-trending faults in the study area can be assumed to be generated from Late Precambrian to Early Paleozoic rifting. Their relative positions and orientations can be inferred from the position of transform faults in figure 5.2. Likewise, the NE/SW-trending terrace faults' positions and orientations can be inferred by the position and orientation of the rift segments in figure 5.2. It is more likely that the NW/SE-trending faults in the study were reactivated from the pre-existing

planes of weakness from transform faults than it is for the NE/SW-trending faults in the study area to be reactivated from planes of weakness left behind by rift segments. The NW/SE-trending faults in the study area are 18° off of what is interpreted to be a potential position for a transform fault in the region. The NE/SW-trending normal faults are more than 30° off the interpreted potential position for the nearby rift segment.

Flexural extension or crustal loading or a combination of both could have generated the orientation of the NE/SW-trending normal faults in the study area. In the case of pre-existing planes of weakness, the high angle normal faults may have been generated from flexural extension as the forebulge of the Arkoma Basin was migrating to the north. DeCelles and Giles (1996) indicates that boundaries of depozones in foreland basin systems can shift laterally through time, that forebulge depozones may be poorly developed or absent, and that forebulge depozones are common sites of unconformity development. For the study area, just prior to the major displacement seen along the NE/SW trending faults at the Mississippian-Pennsylvanian boundary, migration of the forebulge across the study area may have produced flexural extension along the forebulge-foredeep depozone boundary. For the study area the Mississippian-Pennsylvanian boundary is known as a regional unconformity and the forebulge is absent on all interpretations for the study area. Later, at the Mississippian-Pennsylvanian boundary, crustal loading would have generated the bulk of displacement for the NE/SW-trending terrace faults. Crustal loading may have been the sole driving mechanism; however, the trace of the Ouachita Fold Belt is oriented due E/W south of the study area; therefore flexural extension needs to be considered.

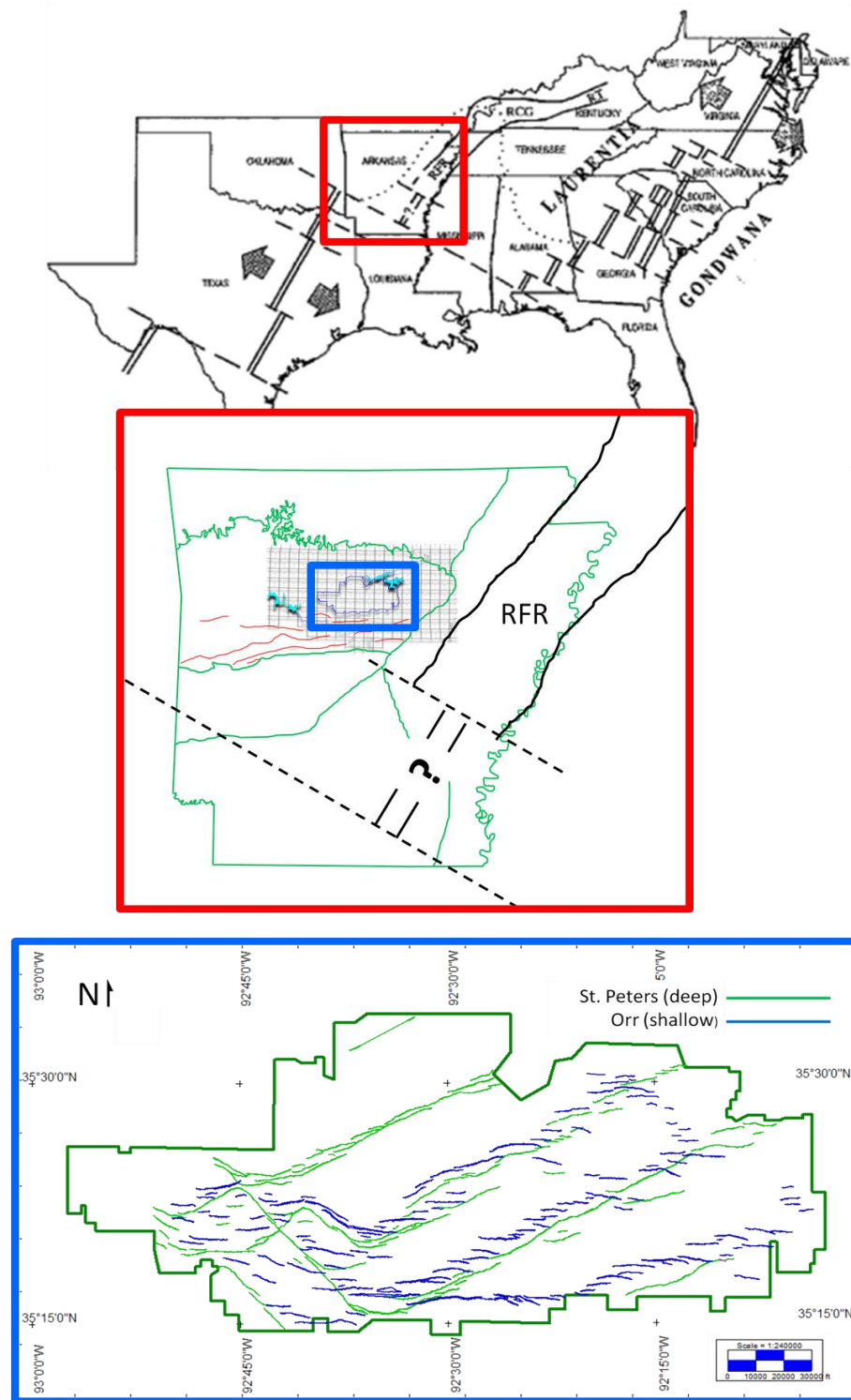


Figure 5.2: (Top) Figure from Dart and Swolfs (1998) showing position of the Early Cambrian, Late Proterozoic continental margin indicating interpreted position of rift segments and transform faults. (Middle) Zoom-in of Arkansas and position of study area; RFR – Reelfoot Rift. (Bottom) Zoom-in of study area and position and orientation faulting.

Finally, reactivation of the NE/SW-trending faults in an oblique manner is essential to generate the en echelon array of shallow normal faults. Dextral slip along the NE/SW faults after deposition of the Lower Atokan units must have been generated from E/W directed compression (figure 4.24) or NE/SW directed extension (figure 5.1) and must have a large enough amount of lateral movement to produce fractures in the overlying section. Both regional extension and compression could generate a local stress field that would align σ_1 in a due E/W direction.

6 Conclusion

Research conducted on the deformation style and timing of the eastern Arkoma Basin has yielded the following results:

1. Three-dimensional interpretation of surface seismic in the study area confirms Van Arsdale and Schweig's (1990) conclusion that there are two separate structural regimes in the eastern Arkoma Basin. There exists a deep set of normal faults that cut the entire passive margin section down to basement and a shallow set of normal faults that penetrate the shallow foredeep Atokan section.
2. Interpreting the subsurface with 3D seismic has enhanced the current understanding of the eastern Arkoma Basin by discovering that there are different orientations and spatial variations of faulting. As previously interpreted, deep faults are oriented in an E/W and NE/SW direction, but also in a NW/SE direction. Also, shallow faults are primarily oriented in an E/W direction with only some deviation.

3. Relative timing for faulting from oldest to youngest in the study area is as follows:
 - a. Deep, down-to-the-southeast normal terrace faults
 - b. Dextral strike-slip movement along the central NW/SE-trending fault
 - c. Reactivation of NE/SW-trending terrace faults in a dextral-slip motion causing an en echelon array of fractures/faults in the shallow section
 - d. Extension generates final amount of normal slip along all deep faults and along the shallow faults structurally above

4. Two structural models hypothesizing actual timing with observed deformation have been generated. Model 1 considers post-Ouachita deformation (figure 4.24) and Model 2 lumps all deformation into pre-Desmoinesian time (figure 5.1). Both models follow the same relative timing proposed in #3. The difference between the two models is late deformation stage timing and cause of final extension.

Going forward, there are 480 square miles (1243 km²) of additional 3D surface seismic data available to add to the eastern portion of this research's designated study area. Supplemental interpretation of this additional data can help to enhance the understanding of the Arkoma foredeep portion of the basin even further.

7 References

- Clark, R. M., and S. J. D. Cox, 1996, A modern regression approach to determining fault displacement-length scaling relationships: *Journal of Structural Geology*, **18**, 147-152.
- Cowie, P. A., and C. H. Scholz, 1992, Displacement-length scaling relationships for faults: data synthesis and discussion: *Journal of Structural Geology*, **14**, 1149-1156.
- Dart, R. L. and H. S. Swolfs, 1998, Contour mapping relic structures in the Precambrian basement of the Reelfoot rift, North American midcontinent: *Tectonics*, **17**, 235-249.
- Dawers, N. H., and M. H. Anders, 1995, Displacement-length scaling and fault linkage: *Journal of Structural Geology*, **17**, 607-614.
- DeCelles, P. G., and K. A. Giles, 1996, Foreland basin systems: *Basin Research*, **8**, 105-123.
- Denison, R. E., 1984, Basement rocks of northern Arkansas, in J. D. McFarland and W. V. Bush, eds., *Miscellaneous publication 18-B, contributions to the geology of Arkansas*, v. II: Arkansas Geological Commission.
- Freund, R., 1974, Kinematics of transform and transcurrent faults: *Tectonophysics*, **21**, 93-134.
- Frezon, S. E., and E. E. Glick, 1959, Pre-Atokan Rocks of Northern Arkansas, Geological Survey Professional Paper, 314 – H.
- Haley, B. R., E. E. Glick, W. V. Bush, B. F. Clardy, C. G. Stone, M. B. Woodward, and D. L. Zachry, 1976, *Geologic Map of Arkansas: USGS and Arkansas Geological Commission Map*, scale 1:500,000.
- Houseknecht, D. W., 1986, Evolution from passive margin to foreland basin: the Atoka Formation of the Arkoma Basin, south-central U.S.A: *Spec. Publs int. Ass. Sediment.*, **8**, 327-345.
- Hus, R., V. Acocella, R. Funiciello, M. De Batist, 2005, Sandbox models of relay ramp structure and evolution: *Journal of Structural Geology*, **27**, 459-473.
- Larsen, P. H., 1988, Relay structures in a Lower Permian basement-involved extension system, East Greenland: *Journal of Structural Geology*, **10**, 3-8.
- Kim, Y., and D. J. Sanderson, 2005, The relationship between displacement and length of faults: a review: *Earth-Science Reviews*, **68**, 317-334.
- Marret, R., and R. W. Allmendinger, 1991, Estimates of strain due to brittle faulting: sampling of fault populations: *Journal of Structural Geology*, **13**, 735-738.

- McFarland, J. D., 2004, Stratigraphic Summary of Arkansas: Arkansas Geological Commission Information Circular 36.
- Morey, D., and G. T. Schuster, 1999, Palaeoseismicity of the Oquirrh fault, Utah from shallow seismic tomography: *Geophysical Journal International*, **138**, 25-35.
- Peacock, D. C. P., and D. J. Sanderson, 1991, Displacements, segment linkage and relay ramps in normal fault zones: *Journal of Structural Geology*, **13**, 721 -733.
- Peacock, D. C. P., 2002, Propagation, interaction and linkage in normal fault systems: *Earth-Science Reviews*, **58**, 121-142.
- Sutherland, P. K., and W. L. Manger, 1979, Mississippian-Pennsylvanian shelf-to-basin Transition Ozark and Ouachita regions, Oklahoma and Arkansas: Oklahoma Geological Survey Guidebook, **19**, 1-13.
- Sutherland, P. K., 1988, Late Mississippian and Pennsylvanian depositional history in the Arkoma basin area, Oklahoma and Arkansas, 1988, Geological Society of America Bulletin, **100**, 1787-1802.
- Stearns, D.W., G. D. Couples, W. R. Jamison, and J. D. Morse, 1981, Understanding faulting in the shallow crust: contributions of selected experimental and theoretical studies, in N. L. Carter, M. Friedman, J.M. Logan, and D. W. Stearns, eds., *Mechanical Behavior of Crustal Rocks, The Handin Volume*: Washington, D.C., Geophysical Union, geophysical monograph 24.
- Thomas, W. A., 1977, Evolution of Appalachian-Ouachita salients and recesses from reentrants and promontories in the continental margin: *American Journal of Science*, **277**, 1233-1278.
- Thomas, W. A., 1989, The Appalachian-Ouachita orogen beneath the Gulf Coastal Plain between the outcrops in the Appalachian and Ouachita Mountains, in R. D. Hatcher Jr., W. A. Thomas, and G. W. Viele, eds., *The Appalachian-Ouachita Orogen in the United States*: Boulder, Colorado, Geological Society of America, *The Geology of North America*, v. F-2.
- Thomas, W. A., 2006, Tectonic inheritance at a continental margin: *GSA Today*, **16**, 4-11.
- Twiss, R. J., and E. M. Moores, 2007, *Structural Geology*: W. H. Freeman and Company
- Van Arsdale, R. B., and E. S. Schweig III, 1990, Subsurface Structure of the Eastern Arkoma Basin: *American Association of Petroleum Geologist Bulletin*, **74**, 1030-1037.
- Watterson, J. 1986, Fault dimensions, displacements and growth: *Pure and Applied Geophysics*, **124**, 366-373.

Whitmeyer, S. J., and K. E. Karlstrom, 2007, Tectonic model for the Proterozoic growth of North America: *Geosphere*, **3**, 220-259.